Spring 2018

Validation of computational methods for fracture assessment of metastatic disease to the proximal femur

Palani Taver Permeswaran
University of Iowa

VALIDATION OF COMPUTATIONAL METHODS FOR FRACTURE ASSESSMENT OF METASTATIC DISEASE TO THE PROXIMAL FEMUR

by

Palani Taver Permeswaran

A thesis submitted in partial fulfillment
of the requirements for the Master of Science
degree in Biomedical Engineering in the
Graduate College of
The University of Iowa

May 2018

Thesis Supervisor: Assistant Professor Jessica E. Goetz

Graduate College
The University of Iowa
Iowa City, Iowa

CERTIFICATE OF APPROVAL

_____

MASTER'S THESIS

_____

This is to certify that the Master's thesis of

Palani Taver Permeswaran

has been approved by the Examining Committee for
the thesis requirement for the Master of Science degree
in Biomedical Engineering at the May 2018 graduation.

Thesis Committee: _____
Jessica E. Goetz, Thesis Supervisor

_____
Nicole M. Grosland

_____
Nicole A. Kallemeyn

_____
Benjamin J. Miller

ACKNOWLEDGEMENTS

First and foremost, I would like to thank my advisor and thesis supervisor, Dr. Jessica Goetz, for her support and guidance throughout my graduate education. Much of my development as an engineer and a researcher is due to her hard work and encouragement. Additionally, I would like to thank Dr. Benjamin Miller for his clinical expertise and his passion for helping those suffering from metastatic disease. Furthermore, I would like to thank Drs. Nicole Grosland, Suresh Raghavan, and Sharif Rahman for their assistance in advancing my graduate education and providing funding. Also, I would like to thank the many other student and staff researchers in the Orthopedic Biomechanics Lab. In particular, I would like to thank Dr. Vijay Permeswaran for sharing his extensive knowledge of finite element analysis and Dr. Jim Rudert for his assistance in developing and performing the mechanical testing reported in this thesis. Finally, I would like to thank my friends and family for their unwavering love, support, and encouragement. None of this would be possible without all of you.

ABSTRACT

Stage IV cancer is characterized by a cancer's ability to metastasize, or spread throughout the body. Metastatic disease in bone is a devastating condition affecting hundreds of thousands of people each year. Stage IV cancer patients suffering from metastatic disease in the proximal femur are at high risk of catastrophic pathologic fracture, an event which severely impacts patient health. Although metrics have been created to assess the risk of impending fracture, they lack specificity in the proximal femoral region. Shortcomings of these metrics further complicate clinical decision making related to prophylactic fixation in these medically compromised individuals.

Fortunately, by using computational modeling to study this at-risk patient population, the likelihood of fracture due to metastatic lesions in the proximal femur can be more accurately assessed to improve clinical decision making. Finite element analysis (FEA) is a computational modeling technique that can non-invasively provide mechanics information to better assess true fracture risk of a given metastatic lesion. Although FEA has previously been utilized to study metastatic disease, lesions were always modeled as spheres or ellipsoids, while true lesion shapes are far more amorphous. It was the focus of this study to validate FEA's ability to predict fracture location in cadaveric femora with realistically shaped experimental metastatic lesions. Off-set torsion, or load applied off-set from the fixed long bone axis, was applied to cadaveric specimens with mechanically induced metastatic lesions, and the resultant fracture location was compared to specimen-specific FEA models replicating the mechanical test. FEA was able to correctly predict fracture locations in five models. Determining fracture risk based on objective mechanical data may more accurate and effective in this patient population.

PUBLIC ABSTRACT

Stage IV cancer is characterized by the cancer's ability to metastasize, or spread throughout the body. Metastatic disease in bone is a devastating condition affecting hundreds of thousands of people each year. Stage IV cancer patients who develop metastatic disease in the upper-most part of the leg, near the hip, have a high risk of a fracture of their leg during normal activities such as walking or climbing stairs. In these very ill patients, surgery to repair a fracture is complicated, the bone does not heal well, and the recovery is much more challenging. Therefore, doctors often make the decision to surgically treat bones with metastatic disease before a break can occur, although they often have to make this decision without knowing exactly what a patient's true risk of fracture may be. This likely results in some patients undergoing invasive surgery that they do not need at a time when they are battling their primary cancer.

Studying this at-risk patient population using a computer modeling technique known as finite element analysis (FEA) permits fracture risk to be more accurately assessed, and hopefully more patients can be spared from invasive surgery. A limitation of previous FEA of metastatic disease is the practice of modeling metastatic lesions as simple 3D shapes. True metastatic lesions are far more non-uniformly shaped. This study focused on confirming FEA's ability to predict fracture location in bones with realistically shaped metastatic lesions. To do that, cadaveric femurs (leg bones) were mechanically tested to fracture under rotational load, and the fracture locations were compared to those predicted by FEA models of the mechanical testing conditions. All models correctly predicted the fracture location. Further FEA study of metastatic disease may provide a more effective assessment of fracture likelihood in this patient population.

TABLE OF CONTENTS

LIST OF TABLES

LIST OF FIGURES

CHAPTER 1: INTRODUCTION AND BACKGROUND

1.1 Metastatic Disease in the Proximal Femur

1.1.1 Cancer and Its Significance

Cancer is one of the most common and debilitating medical conditions in the United States. In 2013, more than 1.5 million people were diagnosed with new cases of cancer at an incidence rate of 439 per 100,000. Over 500,000 people died from cancer, a mortality rate of 163 deaths per 100,000, second only to heart disease. Although there are many different forms, cancers of the colon, lung, prostate, and breast are the most common [1, 2].

Cancer is generally characterized as the abnormal, malignant proliferation of cells in a specific region of the body. These cells invade the surrounding tissue, interrupting normal cellular function and forming masses or tumors. Cancer cells spread quickly through the body or *metastasize* due, in part, to their ability to promote angiogenesis, or the formation of new blood vessels. These blood vessels provide nutrients to the existing tumor while allowing cancer cells access to the rest of the body via the circulatory system [3]. Clinically, cancer severity is ranked as a factor of the tumor size and its spread into the surrounding tissue and/or body, as seen in Table 1-1 [4]. Stage IV cancer is characterized by its ability to aggressively metastasize.

Table 1-1 Clinical Stages of Cancer Severity

Stage 0	Abnormal cells are present but have not spread
Stage I	Small tumor has formed but has not spread anywhere
Stage II	Large tumor has formed but has not spread anywhere
Stage III	Large tumor has spread to the surrounding tissues/lymphatic system
Stage IV	Metastatic or secondary tumors have formed in other areas of the body

1.1.2 Metastatic Disease

Metastatic tumors or lesions can form throughout the body. Lesion formation is heavily influenced by location of the primary tumor. Breast cancers are more likely to metastasize to the spine, lung cancers are more likely to metastasize to the ribs, colon cancers are more likely to metastasize to the liver and lungs, and prostate cancers are more likely to metastasize to the pelvis [5, 6]. Metastasis to bone is the third most common site behind the lungs and liver, and metastatic tumors are far more common than primary bone cancers [7-9]. In 2008, an estimated 279,679 adults in the United States were living with metastatic bone disease. Of this population, 68% were suffering from breast, prostate, and lung cancer as their primary cancer [10].

Metastatic bone disease is a common cause of pain in cancer patients and can lead to severe complications, such as fracture, in the compromised bone [11]. This is due to the interruption of normal bone growth and resorption rhythms by the metastatic cells. Lesions are characterized radiographically by their behavior within the bone; typically, three behavior modes are seen, as shown in Figure 1-1. A lytic bone metastasis exhibits dominant osteoclastic activities in which bone resorption occurs more quickly than formation, causing obvious weakening. A blastic or sclerotic bone metastasis exhibits dominant osteoblastic activities in which bone becomes abnormally dense, leading to a brittle, sclerotic appearance. The third behavior mode is a mixture of lytic and blastic characteristics; however, both behaviors are typically present at varying strengths in most lesions. This leads to amorphous, chaotic lesion shapes and compositions within the bone [12, 13]. Like metastasis location, lesion behavior is also somewhat dependent on the patient's primary cancer. Bone metastases caused by breast and lung cancers are most

often osteolytic; those caused by prostate cancers, however, are typically osteoblastic [14].

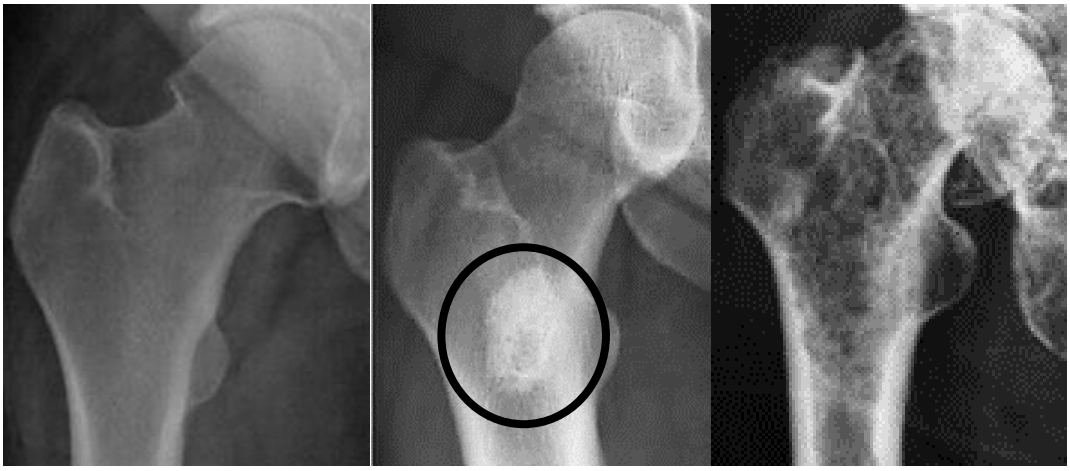

Figure 1-1 Radiographs of a healthy proximal femur (left), blastic lesion (middle), and lytic lesion (right). Radiographically, metastatic lesions are difficult to fully identify, due to their chaotic nature. The blastic lesion (black circle) can be identified by a cloudy area of higher bone density while the lytic lesion can only be identified by the osteoporotic appearance of the bone. Taken from Miller 2015.

1.1.3 Mirels' Scoring and Clinical Decision Making

Unfortunately, Stage IV cancers present significantly lower five-year relative survival rates when compared to Stage I, II, and III cancers. Breast, lung, and prostate cancers show a decrease of 77% (99%-26%), 51% (55%-4%), and 70% (99%-29%), respectively, in five-year survival rates between Stages I and IV [15]. Although these prognoses are relatively poor, surviving patients still wish to return to normalcy as soon as possible after treatment, a path which can be severely hindered by a pathological fracture. Radiation therapy is an effective treatment option to reduce pain associated with a metastatic lesion and risk of pathological fracture; however, only 71% of patients experience a decrease in pain [16-18] from radiation therapy, and the natural remodeling

capability of the surrounding bone is inhibited by radiation, meaning that if a fracture would occur, healing would also likely be impaired.

Prophylactic surgery, as shown in Figure 1-2, is a common treatment option when the risk of pathological fracture is thought to be high. However, due to the compromised health of most Stage IV cancer patients, surgical intervention is only performed on those patients with good longer-term prognoses or those with impending fractures [16, 19]. As these qualifiers are both somewhat ambiguous, the Mirels' scoring system was created to assess metastatic lesion severity and fracture risk to aid clinical decision making. A lesion is scored based upon its location within the body, the fraction of cortical bone thickness involved in the lesion, lesion type, and the patient's self-reported pain, each ranked from 1 to 3 (Table 1-2). The total sum of these categories is a lesion's Mirels' score which represents the fracture risk. Scores of 9 or higher have an increased probability of fracture and are recommended for prophylactic fixation [20].

Table 1-2 Mirels' Scoring System

Score	Lesion Site	Cortical Involvement	Lesion Behavior	Patient Pain
1	Upper Limb	< 1/3 of cortex	Blastic	Mild
2	Lower Limb	1/3-2/3 of cortex	Mixed	Moderate
3	Trochanteric Region	> 2/3 of cortex	Lytic	Functional

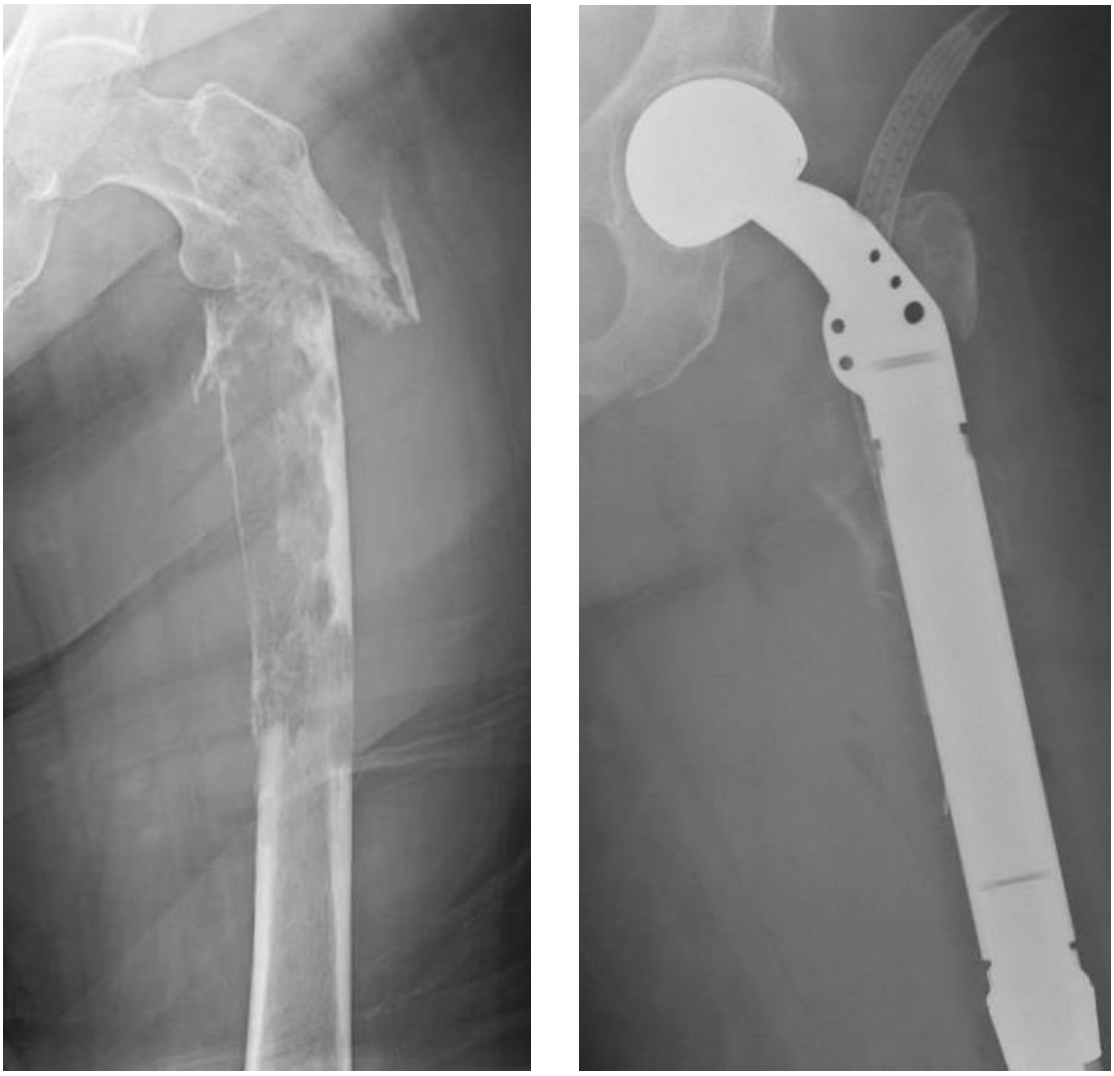

Figure 1-2 Patient suffering from metastatic disease in the proximal femur before and after advanced total hip arthroplasty (THA). Although typical THA or prophylactic surgery is somewhat less aggressive, the highly invasive nature of any preventative prophylactic fixation procedure necessitates good patient prognoses before operation. Taken from Miller 2015.

1.1.4 Mirels' Scoring Non-Specificity in the Proximal Femoral Region

Secondary complications associated with hip fracture lead to higher mortality rates [21], making fractures particularly threatening in a population of medically compromised patients. As evidenced by its high scoring, lesions in the trochanteric or proximal region of the femur are the most structurally severe, accounting for approximately 50% of

fractures caused by bone metastases. Unfortunately, the pain, lesion size, and lesion type metrics in Mirels' scores can be highly variable [22], which has led to a lack of specificity when applying the Mirels' scoring system in the proximal region of the femur [23]. This, and the highly invasive nature of prophylactic fixation in the proximal femur, further complicates the decision clinicians make when weighing a patient's prognosis against their fracture likelihood [24].

1.1.5 Computational Assessment Methods of Metastatic Disease in the Proximal Femur

In an effort to improve data upon which to base clinical decision making, computational analysis techniques are now being implemented in tandem with Mirels' scoring to more accurately assess proximal femur lesion severity and improve clinical decision making. A majority of these techniques focus on computed tomography (CT) imaging-based analyses to quantify bone density at the lesion site and to estimate bone strength from bone density. A relatively new analysis method, CT structural rigidity analysis, calculates locations of maximum weakness in bones to determine bending, torsion, and axial rigidity. These parameters are then compared with those from a gender- and size-matched, healthy femur. A reduction of greater than 35% of any rigidity metric is considered at risk for fracture [23]. However, this is not a widespread analysis technique and the most common computational method used when assessing fracture likelihood in metastatic and healthy femurs remains finite element analysis (FEA).

1.2 Brief Overview of Finite Element Analysis

1.2.1 Theory of Finite Element Analysis

FEA is a computational analysis technique that has been used extensively throughout the fields of structural design, orthopedics, and aerospace for the past 50 years. A validated FEA model can accurately represent a real-world object and predict its mechanical behavior when under multiple loading scenarios. Simply put, FEA allows engineers and researchers to determine the stresses and strains in an object and actively design against failure, without repeatedly, physically destroying the object.

All physical objects can be described by certain laws of physics and mechanics which are governed by partial differential equations. The physical model can be represented mathematically in equation format using what is called the "strong form." However, these equations increase in complexity and become more difficult to solve as model geometry becomes more intricate. Thus, most strong form equations are incredibly difficult, if not impossible, to solve analytically. Integrals, known as the "weak form" equations, are formulated by introducing weighted residuals to the strong form equations. Weak form equations are only valid over the domain of the integration limits, and their solutions are equivalent to the virtual work done on the model. The weak form domain is discretized into multiple integral equations, their solutions calculated at specific points on the model called nodes, and the total solution is summed from the weak form equations at discrete nodal points. Theoretically, as the weak form domains constrict, nodal solutions are calculated closer together and the FEA solution will approach the exact, analytical solution. Interpolation functions further approximate the weak form equations and allow a linear, constitutive, relationship matrix describing the material(s) to be formulated. This

matrix contains material stiffness and characterizes connectivity between all nodes. Thus, a set of linear equations (Kd=F) is formed comprised of the stiffness matrix (K), the nodal displacements (d), and the external forces on the model (F). This set of linear equations is then solved numerically for nodal displacements [25].

1.2.2 Historical Development of Finite Element Analysis

FEA was initially developed in the 1940s and 1950s [26]. During this time, five research groups made significant contributions to the advancement of numerical approximations methods. The first of these, Courant, solved the St. Venant's torsion problem by using linear approximation over discrete points to minimize a stress function on the external boundary. These discrete points were utilized as basic nodes. Second, Argyris developed the matrix theory of structures, introducing the concepts of discrete elements and stiffness matrices. He went on to implement and solve the first rectangular element stiffness matrix in a state of plane stress. Next, Turner derived the truss element stiffness matrix, unique due to its inclusion of object cross-sectional area. Additionally, Turner introduced the idea of a triangular shaped element and defined elements within the global framework, as opposed to the local, element framework. He would go on to implement these global axes into a stiffness matrix. Zienkiewicz and Cheung explored FEA concepts for the first time with regard to non-structural applications and would publish the first textbook popularizing FEA. Finally, Clough observed that solutions to FEA meshes of increasing mesh density converged to the associated analytical solution at known geometries, validating FEA. Moreover, Clough is credited with inventing the name "finite element method", often used interchangeably with FEA [26].

1.2.3 Finite Element Analysis in Orthopedics

Within the field of orthopedics, FEA has been utilized for nearly 50 years. FEA was first implemented in 1972 to calculate stresses in human bones. Initially, FEA models within orthopedics were relatively simple, comprised of basic bone and implant geometries. Contact interactions between objects were difficult to model, and purely linear elastic, isotropic material properties were assumed for complex structures, such as bone. With the popularization of joint arthroplasty, FEA has seen a dramatic increase in utilization, being used to improve the mechanical and functional aspects of orthopedic implant design. As hip arthroplasty was a primary factor driving FEA implementation in orthopedics, the most commonly modeled anatomic location was, and continues to be, the hip [27].

1.3 Femur Anatomy and Biomechanics

1.3.1 The Hip Joint

The hip is a diarthrodial joint within the body which is vital to many everyday human activities, such as gait, stair climbing, and sitting. The hip joint is comprised of the femoral head on the proximal femur and the acetabulum of the pelvis. The hip is an incredibly strong and stable ball and socket joint, supported by various muscular and ligamentous groups attaching to the bony landmarks of the greater trochanter, lesser trochanter, and trochanteric ridge [28-31]. Femur and hip joint anatomy can be seen in Figures 1-3 and 1-4.

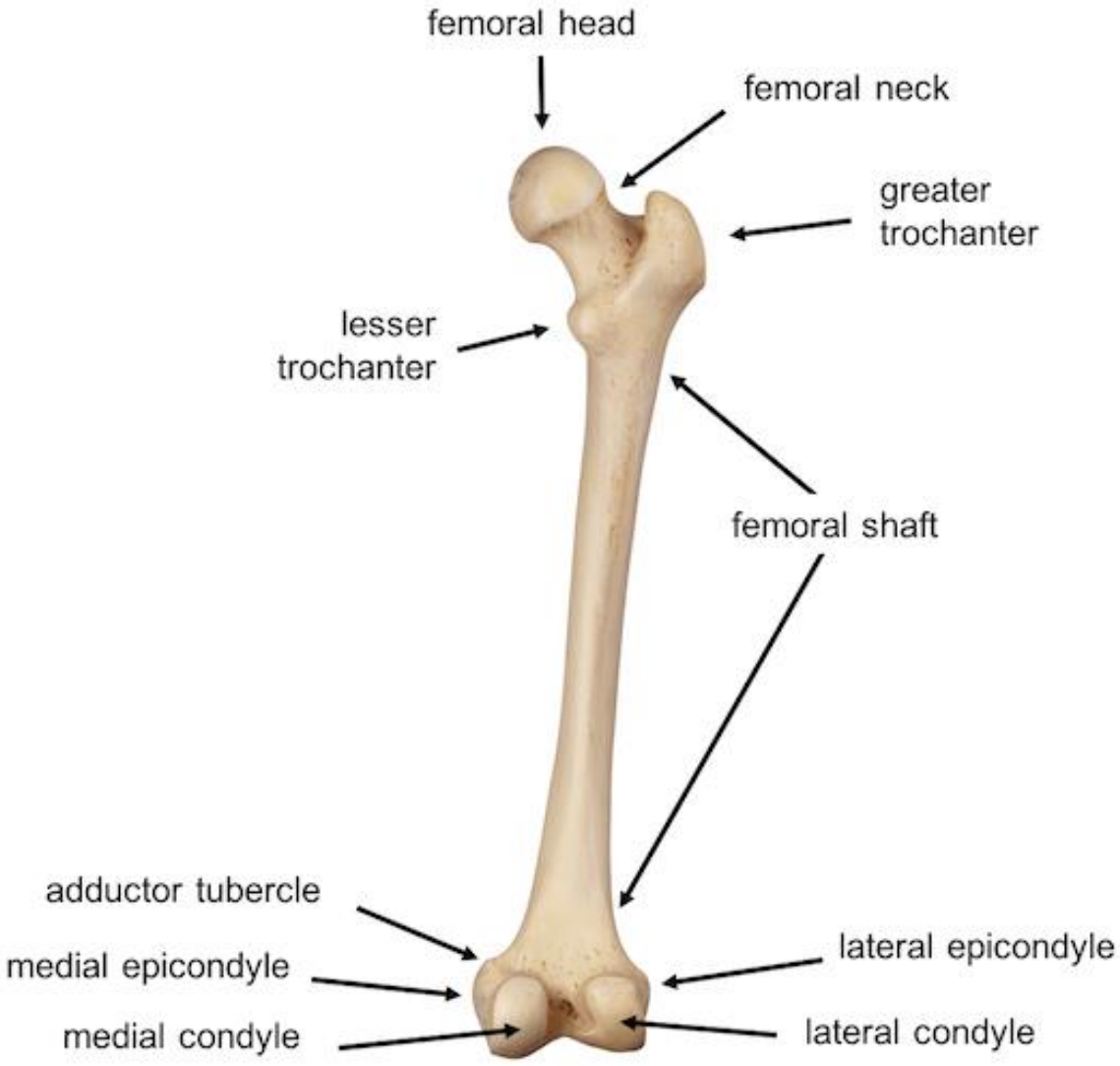

Figure 1-3 Anatomy of the human femur. The region comprised of the femoral head, femoral neck, and greater and lesser trochanters is considered the proximal femoral region. The ridge connecting both trochanters is often called the trochanteric ridge. Taken from Lex Medicus 2017.

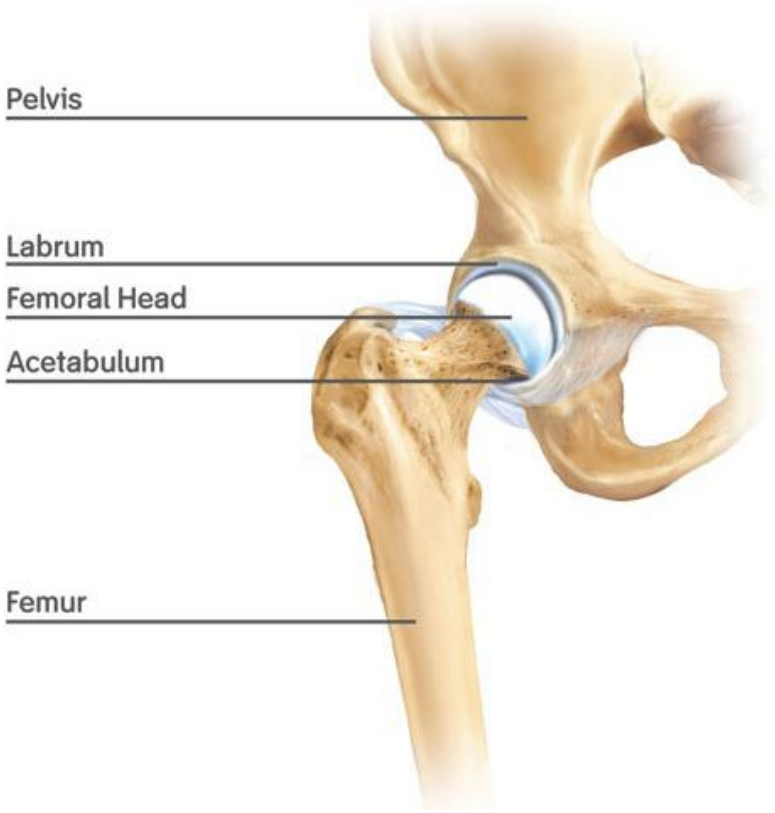

Figure 1-4 Anatomy of the hip joint. The femoral head rotates relatively congruously within the acetabulum. The labrum is a soft tissue structure that further supports the femoral head in the acetabulum. Taken from Schilders 2014.

1.3.2 Bone Structure

There are three distinct bone types relevant to the mechanics of the hip: subchondral bone, cortical bone, and trabecular or cancellous bone. Subchondral bone is a layer of bone below the cartilage in the hip joint. Cortical bone is the dense outer layer of bone and is capable of absorbing large amounts of energy during loading. In this capacity, cortical bone protects the inner structures of the bone. Trabecular bone is made up of a less dense, bony network of trabeculae and provides reinforcement in areas of high stress [32]. While lesion development in the trabeculae can be disruptive to bone strength and function, substantial cortical or subchondral bone involvement is typically indicative of impending fracture [20].

1.4 Finite Element Modeling of the Femur

1.4.1 Healthy Femur Models

The majority of existing FE femur modeling has focused on the healthy or otherwise intact bone. Much of that work has focused on fracture risk inherent in a variety of activities for a variety of patient groups, or considered the effects of a multitude of fixation and implant devices on femur strength. As FE has been used for many years, early models were relatively simple, utilizing coarse meshes and isotropic, homogenous material properties. For example, the model in Figure 1-5 contains 3300 nodes and 667 elements while contemporary models are capable of analyzing several hundred thousand nodes and over one million elements. Additionally, due to improvement of computational hardware and software, time and effort required for such an analysis has been reduced significantly from several days to several hours [33].

Advent of CT scanning in the 1980s allowed FE models to begin incorporating patient-specific geometry and patient-specific, non-homogenous, material properties to bone. By the late 1990s, several research groups had published relationships between CT Hounsfield units and elastic moduli in bone [34]. Of note, is work by the Keyak group whom authored several articles on the process of generating FE models of femurs from CT-based geometry and which included over 150 element sets of distinct elastic moduli. Those models, an example of which can be seen in Figure 1-6, have been used successfully for predicting fracture locations in healthy femurs [35-38].

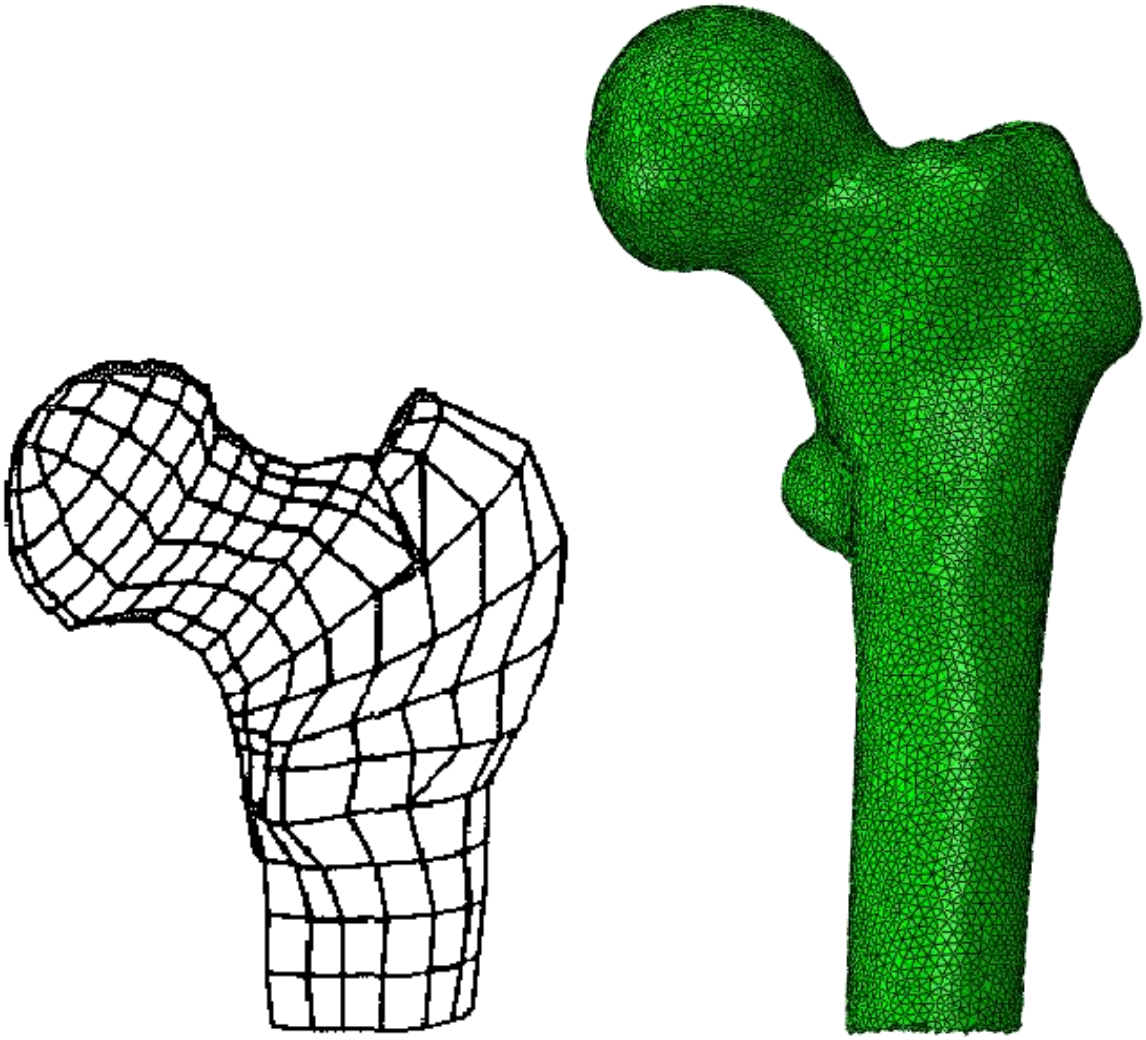

Figure 1-5 Early FE proximal femur mesh (left) and contemporary FE proximal femur mesh (right). Many early models, such as the one on the left, distinguished between cortical elements and trabecular elements to accurately represent the stiff, shell-like nature of the cortex. However, by refining mesh density, bone specific material properties can be applied to each element to replicate bone structure. Taken from Lotz et al. 1991.

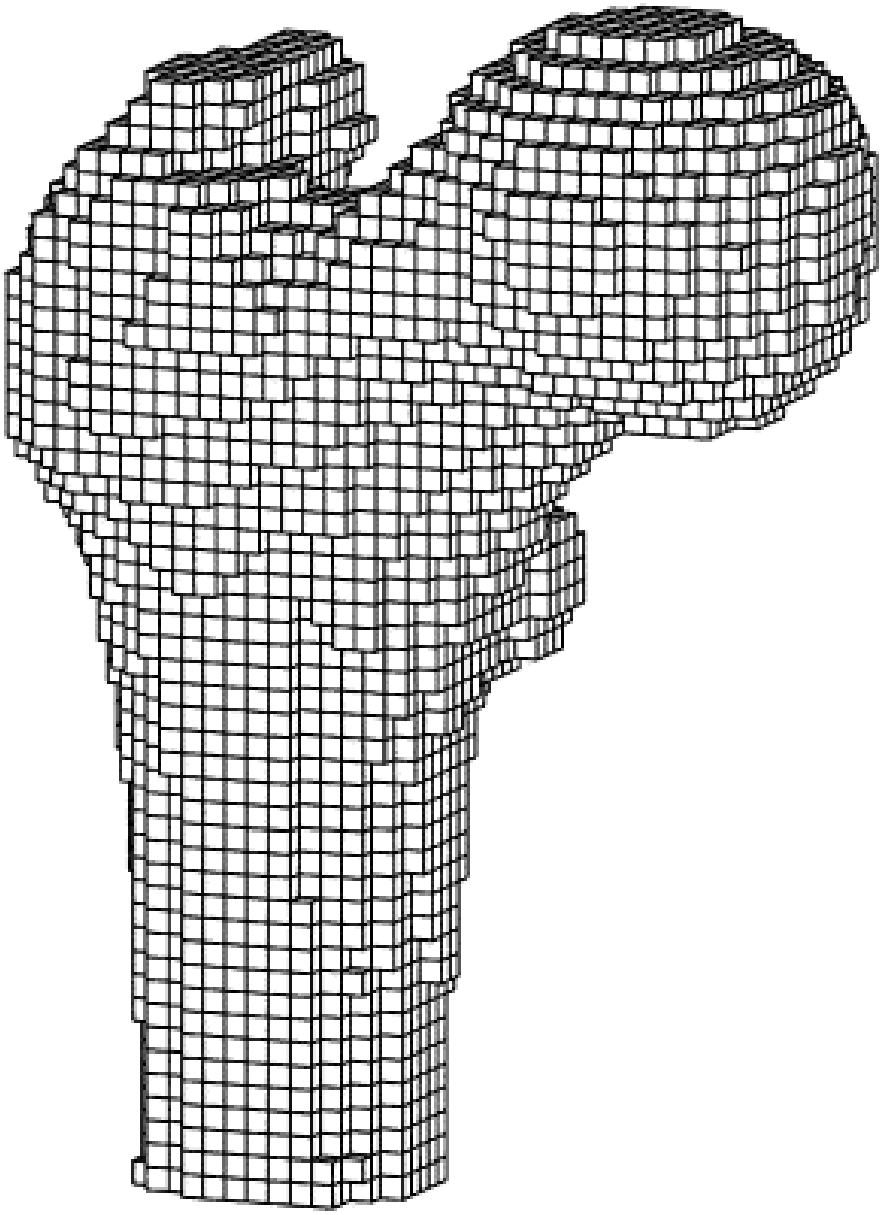

Figure 1-6 A finite element mesh generated directly from the voxels of 3 mm-thick CT slices and therefore comprised of 3 mm cubic elements. Although this model contains over 100 material definitions, the mesh remains coarse when compared to meshes generated for more contemporary models. Taken from Keyak et al. 1997.

1.4.2 Diseased Femur Models

Most previous models assume normal bone strength and intact cortical-trabecular structure relationships. However, such assumptions are inadequate for describing the behavior of metastasis to bone. To date, and despite the relative frequency of metastatic disease in the proximal femur, few femoral FE models containing metastatic lesions have been developed. Of note was a 2007 article by the Keyak research group studying the effect of simulated lytic metastases in a large variety of locations in the femur. 20 mm diameter spherical defects were created in cadaveric proximal femora, and FE models were generated of both the intact and compromised bones. That work determined that defects located in the inferomedial region of the proximal femur had the greatest effect on femoral strength, while those in the superolateral surface had the least effect [39]. However, one key limitation of this work was its study of only spherical defects. Real metastatic lesions are highly amorphous, a behavior which creates greater stress concentrations at the bone-lesion interface than would be seen in simple, geometric defects.

In 2012, Derikx, et al. created FE models from cadaveric femora with simulated lesions of varying size, shape, and location. The fracture location in the FE models and paired mechanical tests of the femora when under axial load were compared. The FE models were able to accurately predict fracture load (R^2=0.9, $p<0.001$), as well as fracture location. However, the only lesion shapes analyzed again were ellipsoids and spheres, as seen in Figure 1-7, which are not representative of clinical lesion shapes. [40].

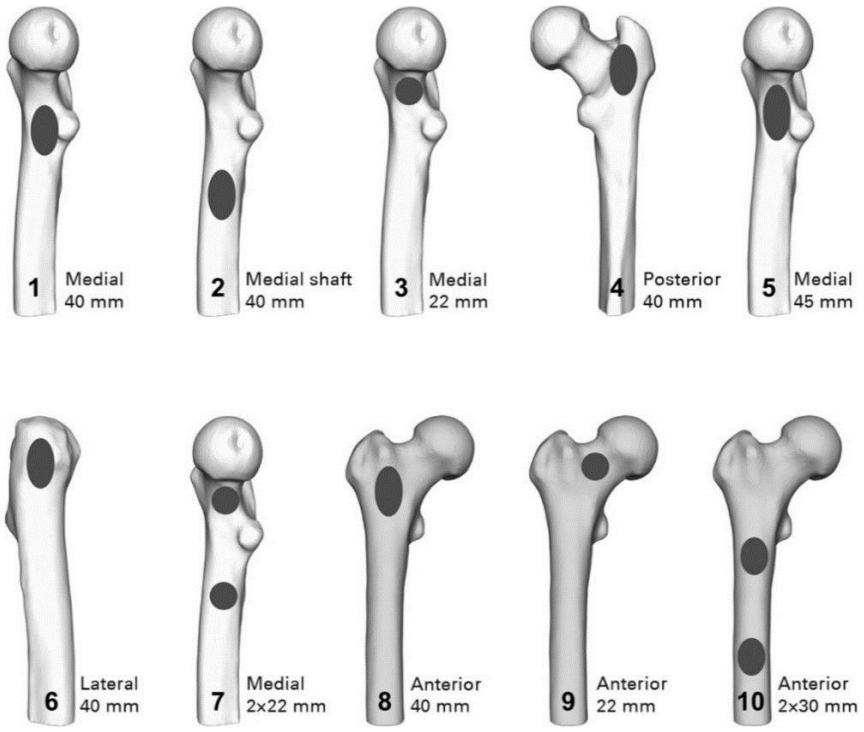

Figure 1-7 Ten simulated lesion locations, shapes, and sizes. Although some groups have investigated the effect of ovoid and spherical defects, clinically encountered lesions are rarely such concise shapes. Taken from Derikx et al. 2012.

The 2015 study by Goodheart, et al. investigated the ability of FEA to predict fracture location in a real patient population. 38 patients (44 femurs total) with metastatic lesions scored from Mirels' 6-12 were selected and followed for four months after initial CT assessment was performed. Five of those femurs fractured within four months, 28 either did not fracture or the patient died without sustaining a fracture within four months, and 11 femurs were stabilized due to high risk of impending fracture as assessed by clinician. It should be noted that in this study not all femurs with lesions scored 9 or above were prophylactically stabilized, as is typically recommended. For the group sustaining a fracture, FEA accurately predicted four out of five failure locations, but also predicted failures in the non-fracture group [41].

1.5 Summary

Metastatic disease in bone is a devastating condition affecting hundreds of thousands of people each year. Although metrics have been created to assess the severity of impending fracture, they lack specificity in the proximal femoral region. This further complicates the clinical decision to prophylactically fix or not, which in turn impacts patient outcomes and quality of life. To date, no validated FEA model of realistically shaped metastatic lesions in the proximal femur has been created. The non-geometric feature of metastatic lesion shape may have serious implications for fracture mechanics. By studying this at-risk patient set using finite element analysis, fracture likelihood in the proximal femur may be more accurately assessed and used to improve clinical decision making. However, this can only occur if the FE models are capturing the true mechanical behavior of the irregularly shaped metastatic lesions.

CHAPTER 2: PREVIOUS STUDY OF METASTATIC DISEASE USING FINITE ELEMENT ANALYSIS

2.1 Correlation of High Mirels' Scores with Fracture Risk in Metastatic Lesions to the Proximal Femur

The first goal of this line of work was to utilize FEA to study increased stresses resulting from metastatic lesions in clinical patients with high Mirels' scores. The purpose was to determine a mechanics-based fracture risk in a patient cohort considered to be at high risk of fracture based on their clinical score. Under IRB approval, 10 patients with metastatic lesions to the proximal femur that rated >= 9 on the Mirels' scoring system were retrospectively analyzed; all patients had received prophylactic fixation for their lesions. The distribution of Mirels' scores among the ten patients was 2 x Mirels' 9, 2 x Mirels' 10, 4 x Mirels' 11, 2 x Mirels' 12.

FEA models of each patient's proximal femur were created. The full details of FEA model creation will be described in detail in Chapter 4. Briefly, clinical CT scans of each patient were extracted from the electronic medical record and patient-specific femur and lesion geometry were manually segmented in OsiriX (Pixmeo SARL, Geneva, Switzerland). These CT scans were acquired for the purpose of determining other possible metastatic lesion sites in the trunk of the body and, as such, typically did not extend distal to the lesser trochanter. Consequently, only proximal femur geometry could be segmented, as seen in Figure 2-1. 3D surface models were generated from these segmentations, aligned to a standard coordinate system, and meshed with tetrahedral elements [42]. Patient-specific material properties were then assigned to each element using CT Hounsfield intensity values. Element yield stresses were also calculated from

CT information to be used in determination of element failure in post-processing. Two different loading conditions were applied to the models: a 750 N (human body weight), single-leg-stance load, and a gait cycle with applied loading obtained from instrumented total hips [42, 43]. Single-leg-stance loading was studied to determine the response of patient-specific FEA models to a simple, low-magnitude, loading condition. Gait was studied to provide a more strenuous activity during which fracture is likely to occur in a compromised femur.

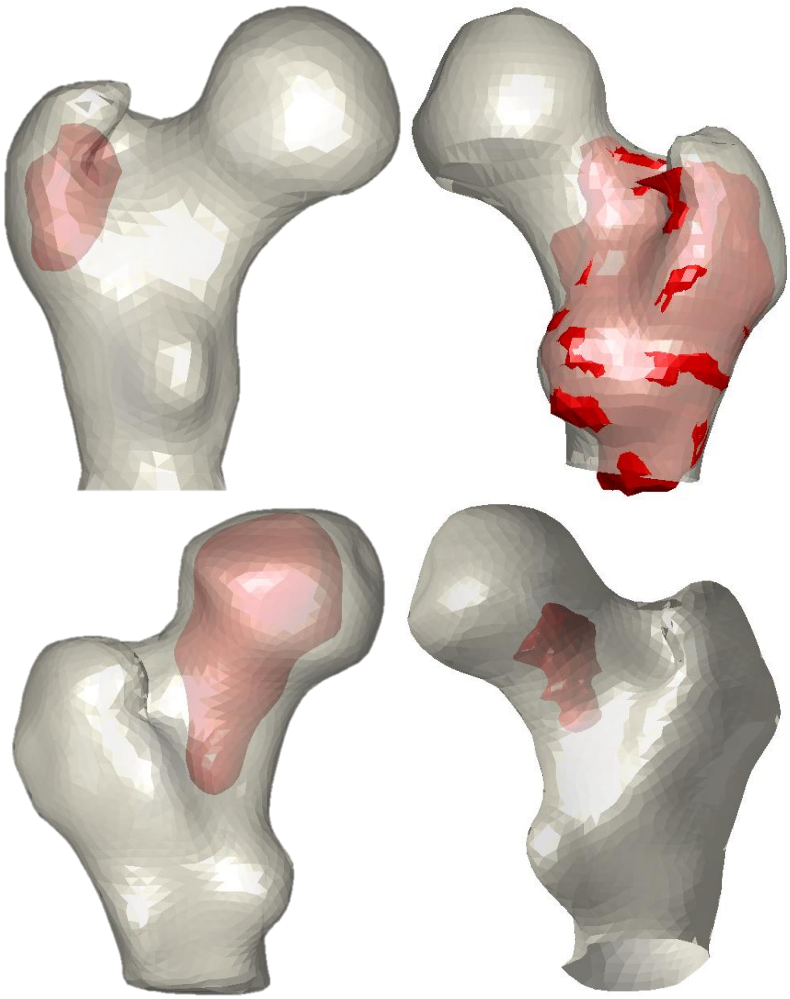

Figure 2-1 Surface models representing a variety of patient-specific geometry and lesions (shown in red). Lesions vary in size, shape, and location despite receiving the same score (11) based on Mirels' criteria. The varying length of bone available from the clinical CT scans is evident.

2.1.1 Percentage of Element Failure during Stance Loading

Our methods of evaluating fracture likelihood were initially focused on assessing the entire proximal femur as a single structure, rather than local fracture characteristics. To evaluate overall likelihood of fracture, each individual element's ratio of yield stress over loaded stress, often referred to as a factor of safety, was calculated [43]. The lower an element's factor of safety, the more likely it was to fail; a factor of safety of one or less indicated element failure. All elements within the lesion space were assumed yielded prior to loading and were excluded from this initial analysis. After determining the total number of failed, non-lesion elements, the percentage of element failure, defined by the ratio of the number of failed non-lesion elements divided by the total number of non-lesion elements, was calculated (Table 2-1). Few models developed element failure under this single-leg-stance loading condition, and those few models that did indicate failed elements showed less than one percent of the elements had failed. Correlation between a model's Mirels' score and percentage of element failure was low at $R^2 = 0.042$ [44].

Table 2-1 Percentage of Element Failure for Varying Mirels' Scores during Stance

Model Mirels' Score	9	9	10	10	11	11	11	11	12	12
Percentage of Element Failure (%)	0	0	0	0.006	0	0	0	0.456	0	0.079

Element factor of safety was then averaged across all elements in an attempt to quantify fracture likelihood of the entire model. However, because the majority of elements in the model possessed large factors of safety caused by a lack of direct loading, and due to the large number of elements in each mesh (on the order of several hundred thousand elements), the effect of failed elements was obscured when averaged across the entire model. Thus, this metric was abandoned, and it was concluded that Mirels' scoring does not directly correlate with high fracture risk during low-magnitude loading [44].

2.1.2 Percentage of Element Failure during Gait Cycle Loading

Due to the extremely small number of yielded elements found during stance loading, it was thought that a more strenuous activity, such as gait, may be more likely to cause fracture. The force vectors experienced by the hip during the stance phase of gait from heel strike to toe off [42] were discretized into thirteen FEA loading steps and applied to each model. The percentage of total failed elements was again calculated for each model at each gait cycle loading increment (Table 2-2). Correlation coefficients between each model's Mirels' score and the percentage of failed elements were also calculated at each gait cycle loading increment. Little correlation was found at any time during the stance phase of gait. It was concluded that the total percentage of failed elements was too broad of a metric to assess fracture risk given that metastatic lesions are more likely to affect load carriage in local regions than in the entire femur (Figure 2-2). Rather than characterizing the entire bone, specific locations of element failure and their corresponding fracture risk needed to be identified [45].

Table 2-2 Percentage of Failed Elements for each FE Model during the Stance Phase of Gait

Mirels' Score	Percentage of Element Failure (%)												
Gait Steps	1	2	3	4	5	6	7	8	9	10	11	12	13
9	0	0	0	0	0	0	0	0	0	0	0	0	0
9	0	0	0	0	0	0	0	0	0	0	0	0	0
10	0	0	0	0	0	0	0	0	0	0	0	0	0
10	0	0	0.008	0.003	0	0	0	0	0	0	0	0	0
11	0	0	0	0	0	0	0	0	0	0	0	0	0
11	0.784	1.159	1.340	1.182	0.884	0.575	0.347	0.849	1.083	1.177	1.187	1.030	0.837
11	3.747	5.167	6.337	6.676	5.714	5.028	4.876	4.813	4.633	4.827	4.509	4.162	3.795
11	0.142	0.325	0.734	0.551	0.292	0.125	0.058	0.025	0.025	0.067	0.042	0.042	0.025
12	0	0	0	0	0	0	0	0	0.001	0.001	0.001	0	0
12	0.078	0.098	0.112	0.114	0.108	0.097	0.085	0.083	0.081	0.088	0.087	0.079	0.069

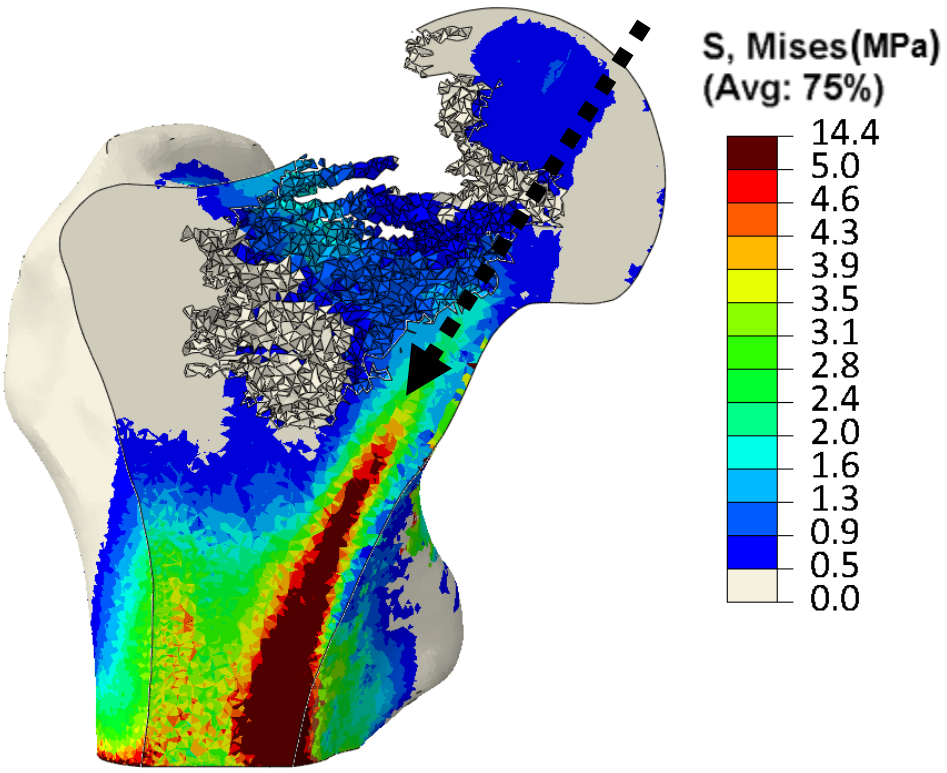

Figure 2-2 Coronal cross-section of von Mises stress in an FEA model with a Mirels' 10 lesion during a later stage of gait. Elements of the lesion have been removed to visualize the stresses relative to the extent of the lesion. The normal load carriage through the femur, visualized by a black arrow, is interrupted by the lesion which shifts load-bearing to other locations to compensate.

2.1.3 Critical Failure Volume during Gait Cycle Loading

To identify focal locations of element failure, a contiguous element analysis was conducted on the data from the FEA models of walking gait. Similar analyses in the literature have shown that contiguous element volumes of 81 mm^3 or greater accurately predict fracture. This specific value was empirically determined as the total volume of contiguous 3-mm cubic elements that needed to have computationally failed in order to match physical bone failure [36]. To calculate contiguous failed element volumes in this work, all element stress and location data were imported into MATLAB. The element with the smallest factor of safety, which corresponded to the element undergoing the most extreme yield, was identified. It was assumed that fracture would initiate at this element. Then, any failed element which shared nodes with the original failed element was added to a failed element set. This process was repeated recursively until no new elements were identified as contiguous. The fraction of the total volume of this group of failed elements over 81 mm^3 was calculated. [35]. This relative fraction of critical failure volume was plotted over the gait cycle for each model (Figure 2-3). Using this metric, only two of the ten patient models exceeded critical failure volume. All other models had less than one tenth of a critical volume needed to fracture. These results lend credence to the concept of catastrophic fracture propagation in these patients; models experience large amounts of localized failure, indicative of an impending fracture, or almost no element failure. Correlation coefficients relating model Mirels' scores and the fractions of critical failure volume were calculated at each gait step. Again, there was little correlation at any point in the gait cycle, further substantiating the perception that high Mirels' scores do not directly correlate to a higher risk of fracture [46].

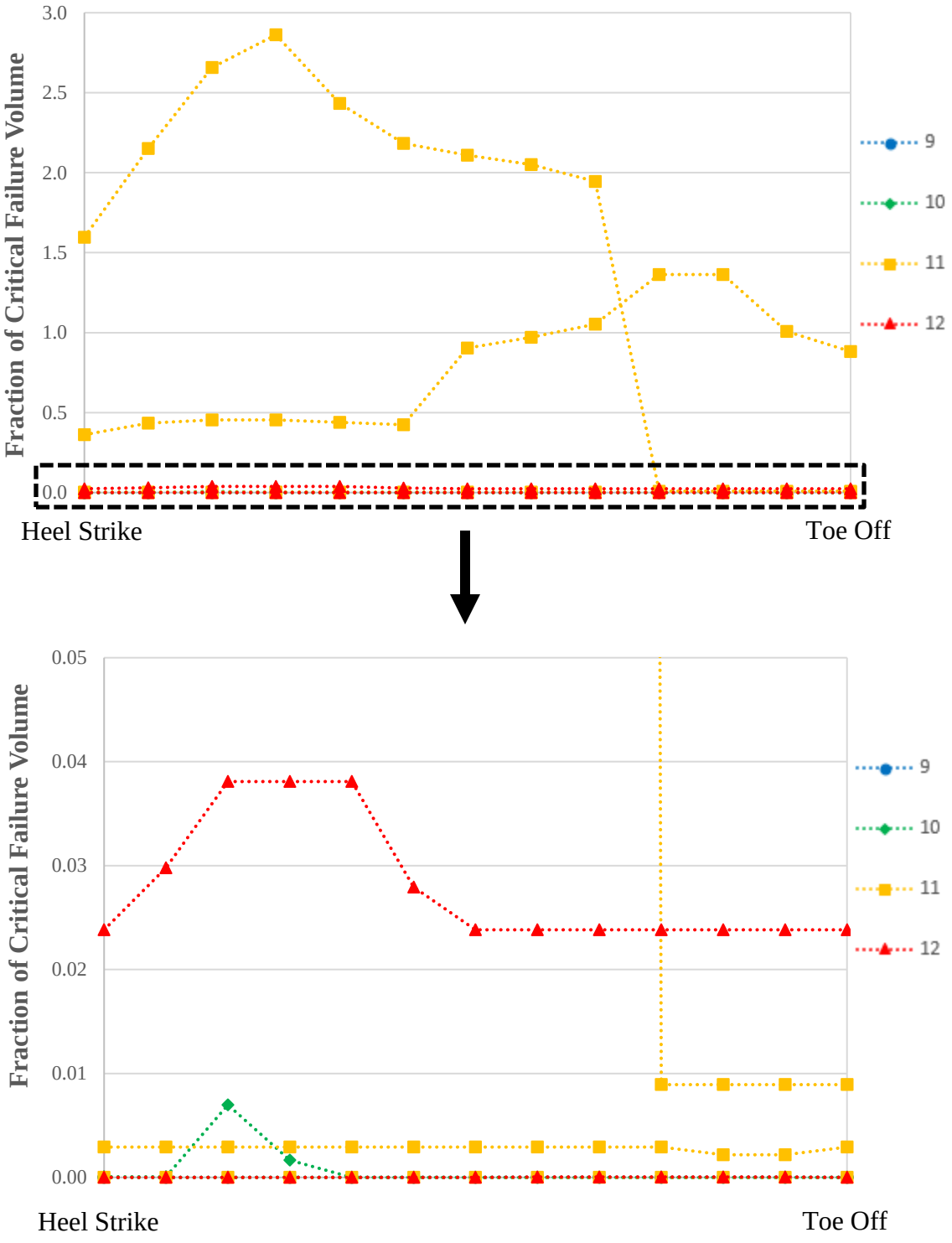

Figure 2-3 Fraction of critical failure volume versus progression through stance phase of the gait cycle. Many models experienced no element failure and overlap at 0.

2.1.4 Interpretation and Discussion

After analysis of femur mechanics using the percentage of failed elements metric and more localized analysis using the fraction of critical failure volume metric, it was concluded that high Mirels' scores did not directly relate to specific mechanical risks. However, there were several major limitations to this work. First, this work was a study only of patients with high Mirels' scores. It is possible that the inclusion of additional patients with lower risk proximal femur lesions may improve correlation between stress-based fracture prediction and Mirels' score. Additionally, CT scans were only available for the proximal 110-130 mm of each femur. As seen in Figure 2-2, this created stress risers near the distal boundaries. The inclusion of the full or partial femoral shaft could reduce these stress risers and provide more accurate stress distributions. Also, the application of more strenuous loading patterns, such as sit-to-stand or stair climb, could increase the amount of focal element failure experienced by each model. Finally, failure was assumed to occur at the element undergoing the largest yielding. However, this extremely yielded element could be the result of poor element quality during mesh generation or located at the previously mentioned distal boundary stress risers, both of which would create difficulty when determining the contiguous element groups.

Despite these limitations, after the inclusion of actual lesion geometry and material properties, only 20% of FEA models indicated stress patterns that would likely fracture. This may suggest that the remaining 80% of models (patients) were not at a high risk of fracture during gait based on mechanical analysis. However, without validation of our fracture criteria in our particular FE modeling approach, it is difficult to extend this finding to the clinical setting.

CHAPTER 3: MECHANICAL TESTING OF CADAVERIC FEMORA WITH ARTIFICIAL DEFECTS

3.1 General Validation Methodology and Selection of Loading Activity

This validation study was designed to assess our FEA models' ability to predict fracture location in cadaveric femora with simulated metastatic lesions. Mechanical testing was performed on cadaveric human femora with realistically shaped metastatic lesions, and corresponding FEA models were created of each individual experiment. Loading and boundary conditions similar to mechanical testing were applied to the FEA models, and fracture location was predicted using the contiguous element failure volume analysis technique. Fracture locations were compared between the mechanical testing and FEA. In order to provide relevant results, the mechanical testing chosen needed to load the proximal area of the femur, specifically the neck and trochanteric region, in an experimentally reproducible manner. Additionally, it was desired that the loading paradigm be translatable to a real-world activity. Torsional loading of the femur is often seen in activities such as gait, sit-to-stand, and stair-climb [47-49]. Off-set torsion, or torsion created with the load applied off-set from the fixed long bone axis, was chosen as it was easy to implement experimentally and it replicates loading that can develop during real-world activities.

3.2 Specimen Collection and Preparation

3.2.1 Cadaveric Femur Dissection

Five cadaveric lower extremities were obtained from the University of Iowa Department of Orthopedics & Rehabilitation Skills Laboratory. The femora were dissected out of the surrounding muscle and soft tissue and wrapped in saline-soaked, paper tissue for transport to the Orthopedic Biomechanics Laboratory specimen freezers for storage. Specimen donor information is shown in Table 3-1. CT scans of each specimen were obtained on a Siemens Somatom Force dual source CT scanner with slice spacing of 512 x 512 x ~900 (varied depending on femur size) which, at slice sizes of 0.2246 mm and 0.5 mm, corresponds to 115 mm x 115 mm x ~450 mm. Each specimen remained wrapped in saline-soaked, paper tissue during scanning. All scans included calibration objects to assess CT intensity-bone density relationships in future studies.

Table 3-1 Specimen Donor Information. No information was available for specimen #5

Specimen Number	Age at Death	Cause of Death	Abnormalities
1	32	Breast Cancer, Liver Failure	Metastasis to pelvis and brain
2	68	ALS	-
3	78	Breast Cancer	Metastasis to liver and heart
4	81	Brain Degeneration	-
5	-	-	-

3.2.2 Distal Femur Potting

To easily manipulate the femur during creation of the metastatic lesions in the proximal femur, and to provide a suitable surface for clamping during mechanical testing, the distal region of each femur was potted in polymethylmethacrylate (PMMA). First, metal screws were embedded into the femoral condyles and into the distal portion of the

femoral shaft, as seen in Figure 3-1. These screws also oriented the femoral shaft vertically within the molding container. During potting, each femur was rotated such that the femoral neck was parallel to the edge of the potting box and clamped. This orientation was chosen to replicate off-set torsional set-ups seen in literature and can also be seen in Figure 3-1.

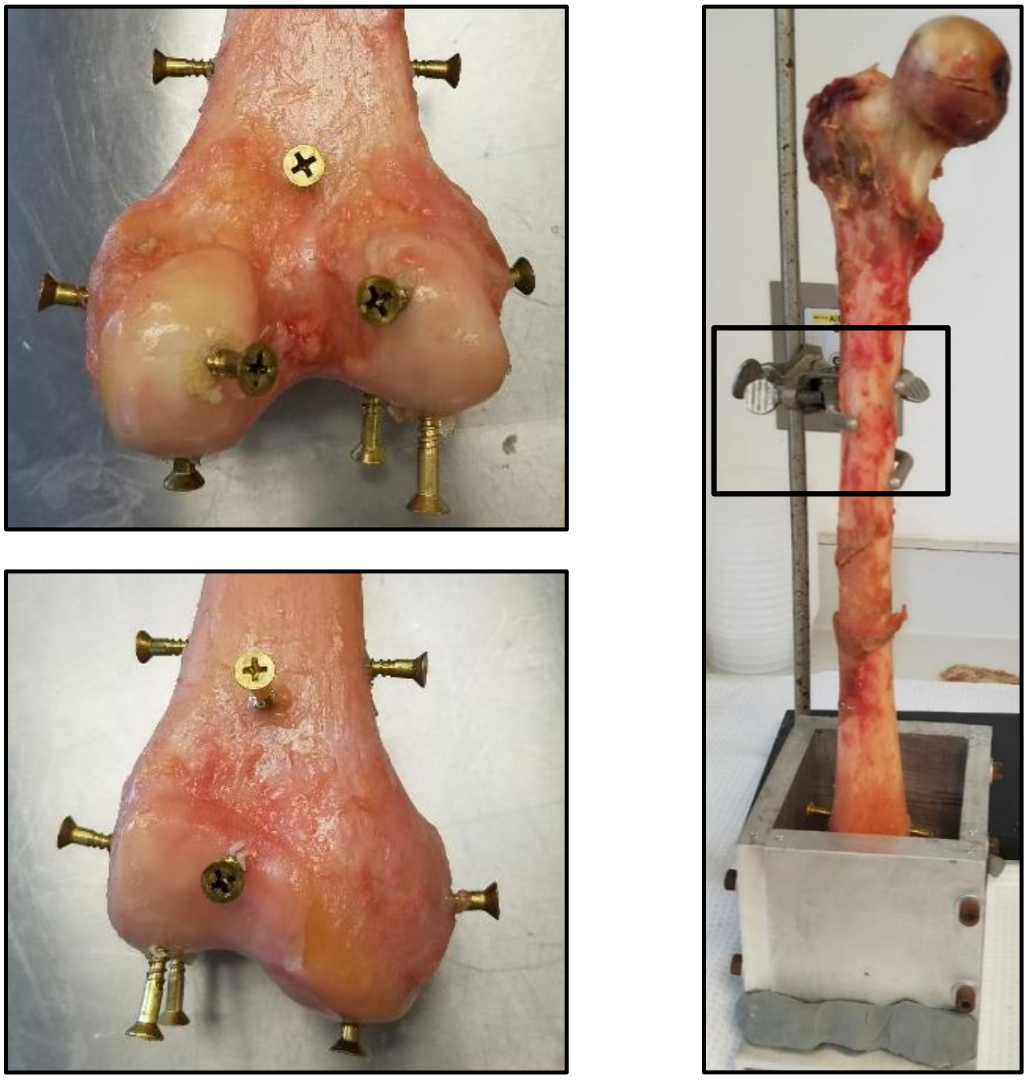

Figure 3-1 Metal screws inserted into the femoral condyles and distal femoral shaft (left) and a cadaveric femur oriented vertically for potting (right), with the femoral neck parallel to the front visible surface of the potting box. To ensure proper orientation, the femora were held in place by a clamp, highlighted in the image.

PMMA is created by combining a two-part epoxy. Immediately after mixing, PMMA briefly existed as a liquid, able to be poured into the potting box. Shortly thereafter, the PMMA began to polymerize, forming solid blocks around the distal femur, seen in Figure 3-2 [50]. The femora were preserved with saline solution throughout this process.

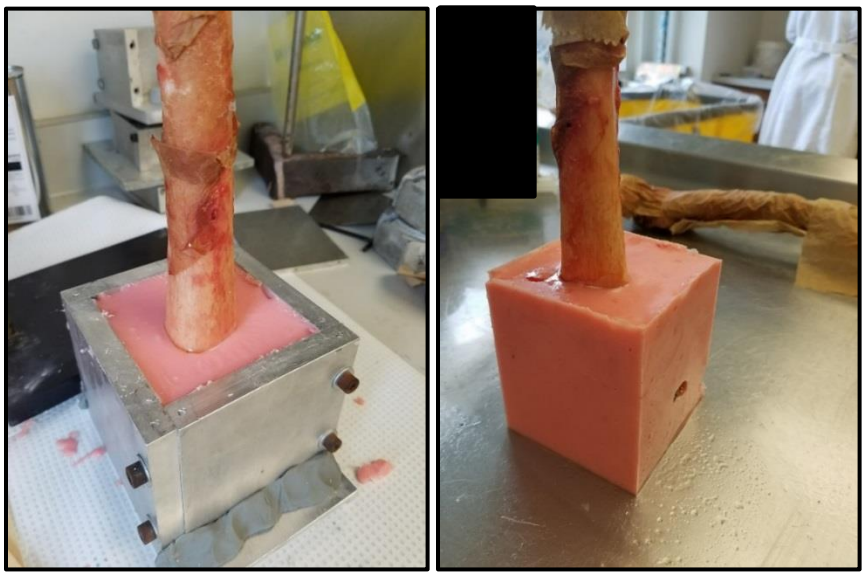

Figure 3-2 PMMA during the polymerization or "curing" process. PMMA heats significantly during curing and can be damaging to soft tissue.

3.2.3 Proximal Femoral Head Cast

During mechanical testing, application of load was distributed across the anterior femoral head via custom-molded PMMA cups. A molded cup was created for each specimen to ensure uniform load distribution over the femoral head during testing. After distal potting, the femoral head of each specimen was placed anterior-side down into a shallow molding container. The entire specimen was raised or lowered, as seen in Figures 3-3 and 3-4, to achieve as much PMMA coverage of the head as possible while minimizing contact with the neck, and weights were placed on the distal pot to maintain stability.

Figure 3-3 Potted femur positioned for head cast creation. Metal plates were utilized to raise or lower the specimen.

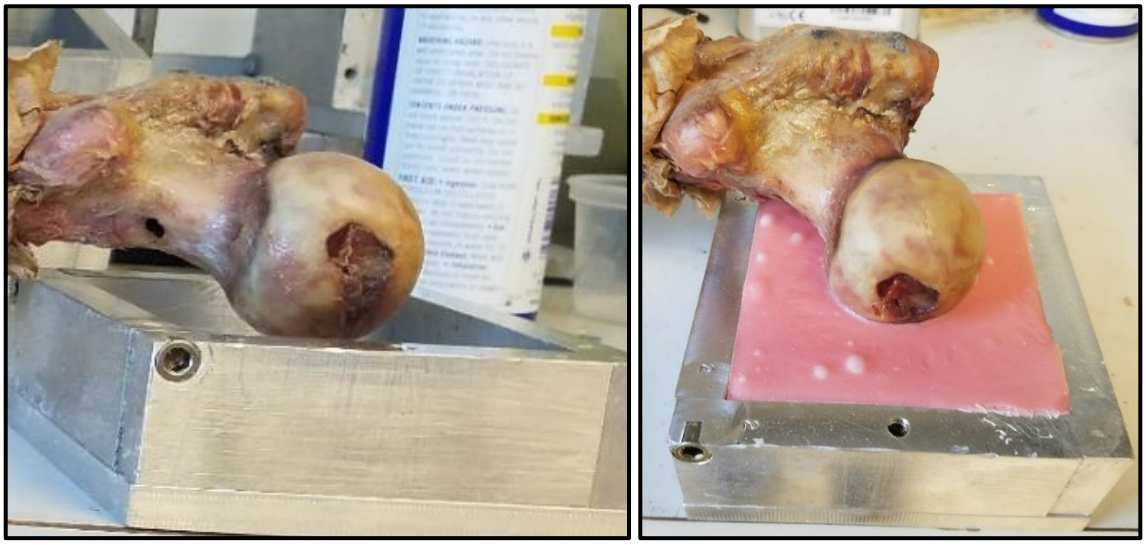

Figure 3-4 Potted femur positioned before (left) and after (right) head cast creation. The entire femur was raised to allow only the femoral head to contact the PMMA.

Petroleum jelly was applied to the femoral heads to allow for ease of removal once the PMMA was cured. PMMA was mixed and poured into the molding container, creating specimen-specific Head Casts. During use for load application, it was possible for the lateral edges and faces of the head casts to impinge upon portions of the intertrochanteric region and the femoral neck. To eliminate any possibility of impingement during testing, the lateral portions of the femoral head casts were cut away, as seen in Figure 3-5.

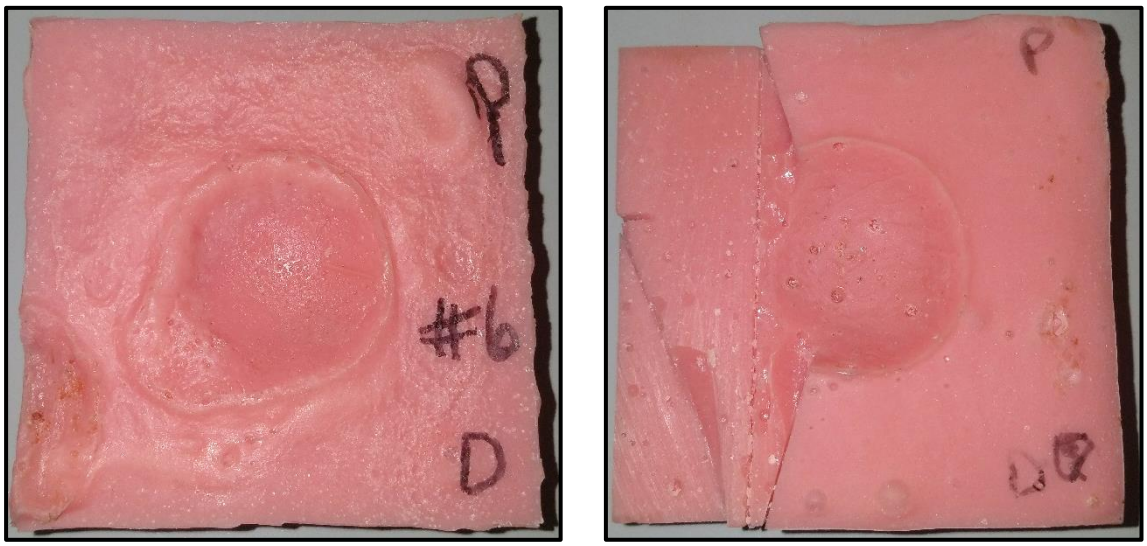

Figure 3-5 Head cast before possible impingement sites have been removed (left) and after (right). The cups were marked "P" and "D" for proximal and distal, respectively, to remove any ambiguity when inserting the head casts into the MTS apparatus.

3.2.4 Lesion Creation

As nearly all femurs with metastatic disease modeled to date have studied spherical or ellipsoid lesion shapes, a point of emphasis in this work was creating lesions of a similar shape to those seen clinically. Two primary lesion types were created: those in the lateral trochanteric region with minimal cortical and significant trabecular involvement, and those in the inferomedial neck region with significant cortical and

trabecular involvement. Similar methodologies were utilized in creating both types. First, a drill bit, approximately 3.175 mm in diameter, was used to penetrate the cortical shell in the greater trochanter or the femoral neck, depending on lesion type, as seen in Figure 3-6. This hole provided access to the trabeculae beneath the region of interest and was slowly enlarged until larger tools could be inserted. A combination of surgical rongeurs, curettes, and side-cutting drill bits were utilized to core out the trabecular bone in somewhat arbitrary patterns, to mimic the chaotic nature of metastatic disease; these tools can be seen in Figure 3-7. Specimens were preserved with saline solution throughout this process.

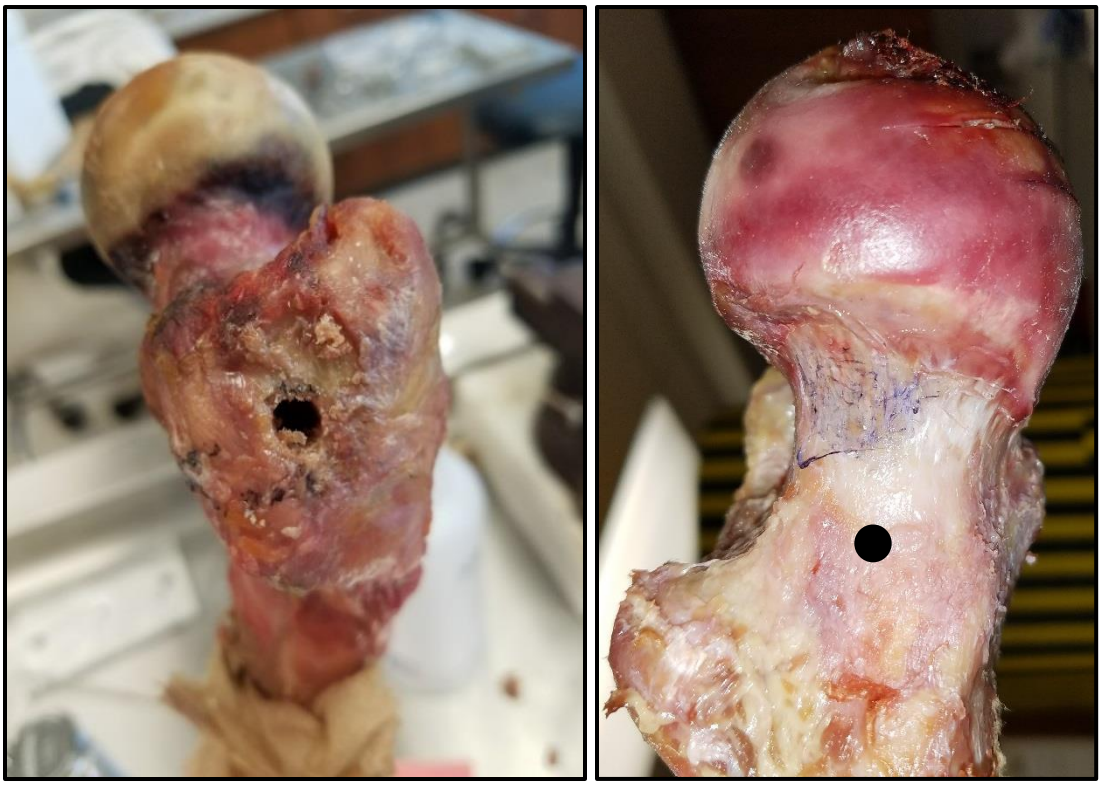

Figure 3-6 Trochanteric (left) and femoral neck (right) access points for removing trabecular bone.

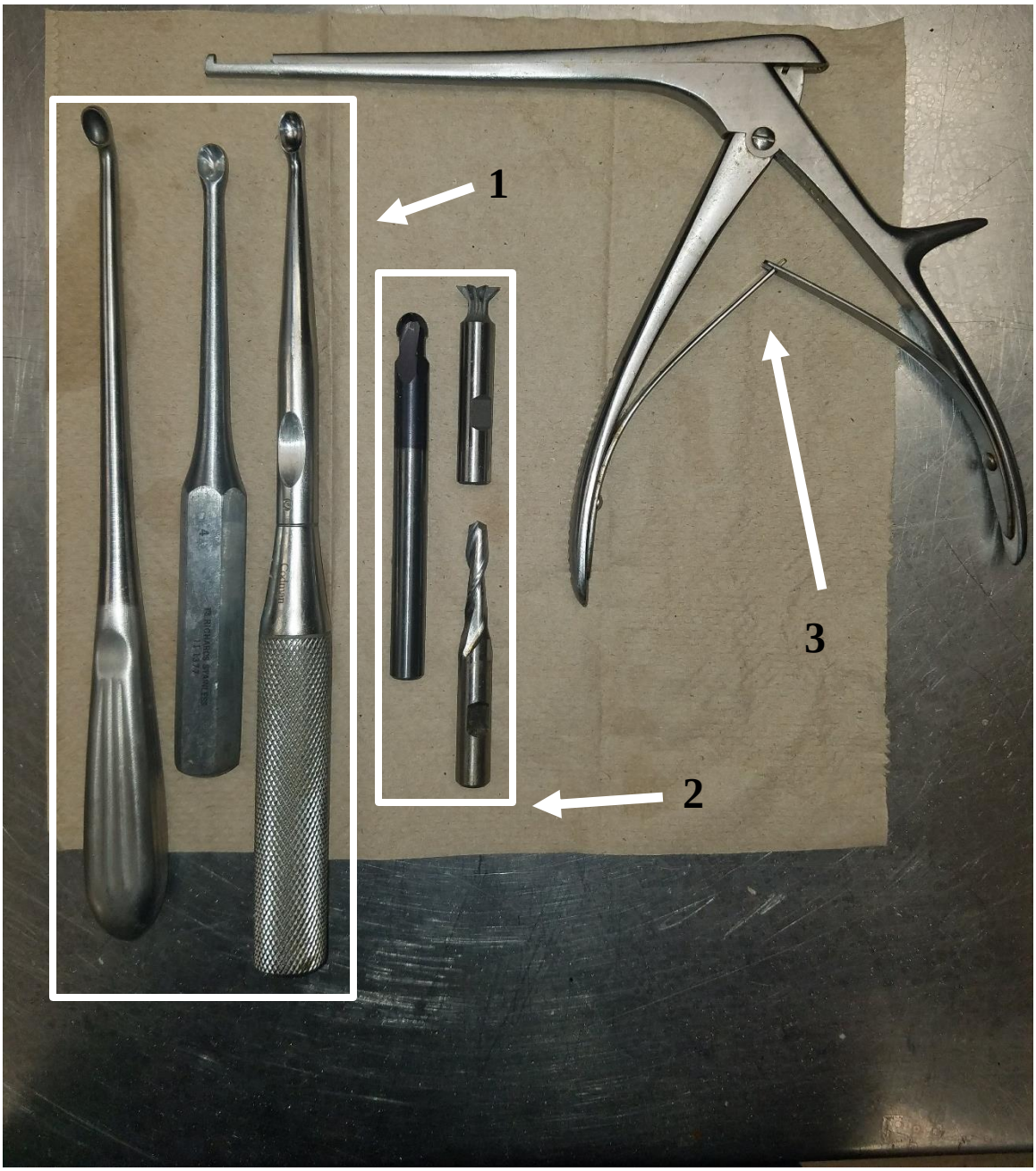

Figure 3-7 Tools utilized for lesion creation. 1 = Surgical curettes-used primarily for scraping out trabecular bone, 2 = Specialized drill bits-used primarily for widening holes where curettes could not fit, 3 = Surgical rongeurs-used primarily for punching out cortical bone after the underlying trabeculae was removed.

Of the five cadaveric specimens, three had lesions created in the trochanteric region with varying amounts of cortical involvement in the neck and large areas of trabecular bone removed. The remaining two specimens had lesions with large amounts of cortical bone removed in the inferomedial neck and varying amounts of the surrounding trabeculae affected. Individual lesion shapes can be seen in Figures 3-8 through 3-12. Lesion shape was fully verified via CT imaging using the same scanning parameters as the pre-lesion scans. However, no calibration objects were included as the fundamental quality of the bone had not been significantly altered during lesion creation.

Figure 3-8 Simulated lesion in cadaveric specimen #1 viewed from the inferomedial aspect. This lesion was characterized by a large perforation of the cortical shell in the neck, near the greater trochanter, and substantial trabecular damage. This lesion will be referred to as “large blowout”.

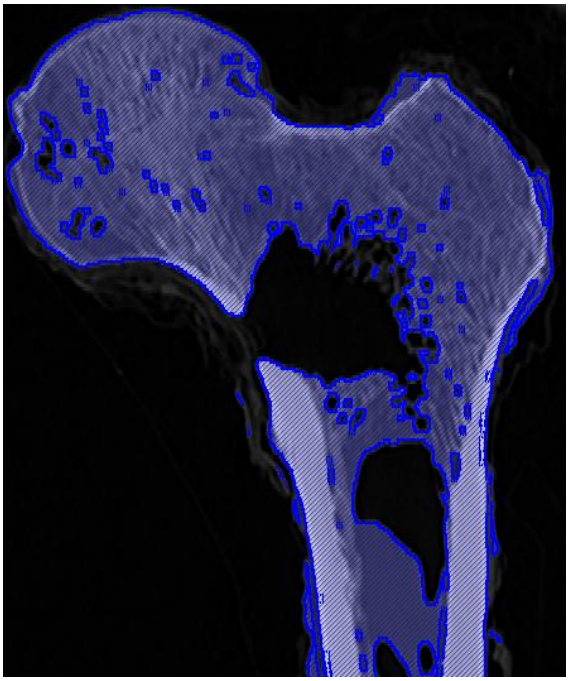

Figure 3-9 Simulated lesion in cadaveric specimen #5. This lesion was characterized by a perforation of the cortical shell in the neck, near the greater trochanter, and significant trabecular damage. This lesion was created as a scaled-down version of "large blowout" and will be referred to as "small blowout".

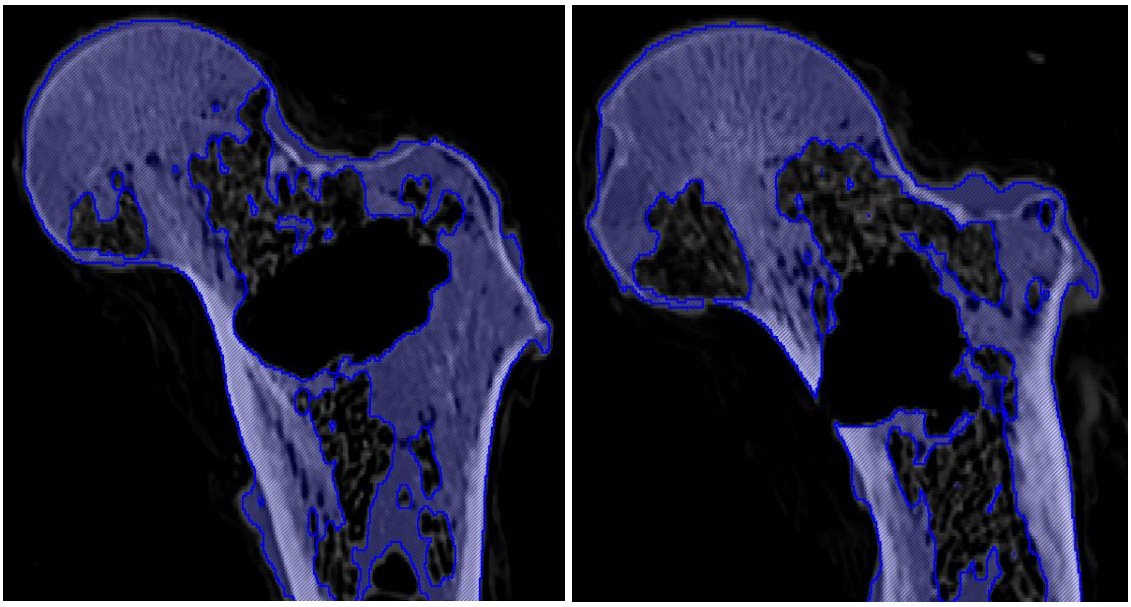

Figure 3-10 Simulated lesion in cadaveric specimen #2. This lesion was characterized by a fairly small perforation of the cortical shell in the neck, significant thinning of the cortical shell around the perforation, and substantial trabecular damage in the intertrochanteric region. This lesion will be referred to as "combination".

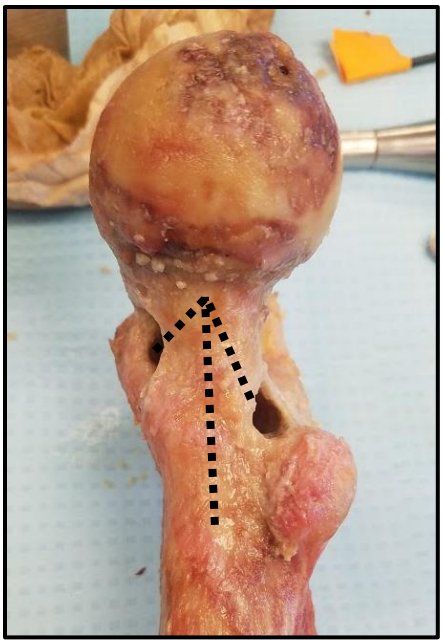

Figure 3-11 Simulated lesion in cadaveric specimen #3 viewed from the inferomedial aspect. This lesion was characterized by two lesion paths extending from the greater trochanteric access point to the cortical shell straddling the neck. An additional path was extended from the access point distally into the IM canal. This lesion will be referred to as "tortuous".

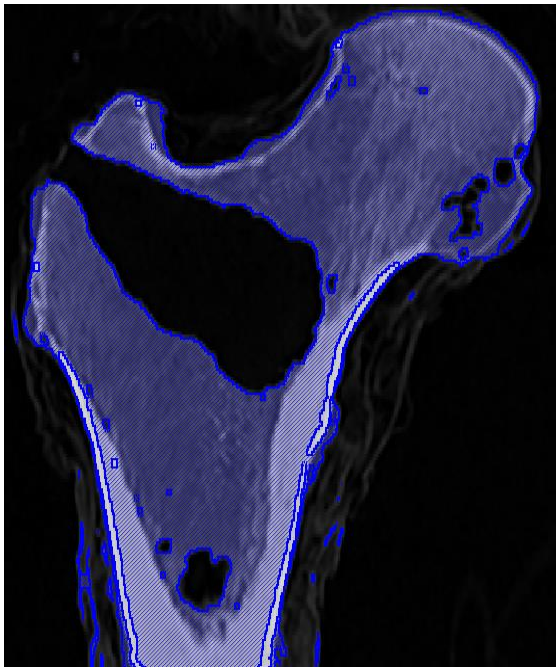

Figure 3-12 Simulated lesion in cadaveric specimen #4. This lesion was characterized by a large amount of trabecular involvement in the intertrochanteric region and little cortical involvement, besides the access hole. This lesion will be referred to as "lateral".

3.3 Mechanical Testing Set-up

Off-set torsional testing was comprised of three points of contact between the testing apparatus and the femur. First, the distal femoral region was clamped rigidly at a height such that the long bone axis was parallel to the testing surface [47-49, 51]. Due to variation in femoral version, the femoral neck was often not perfectly parallel with the testing surface, as seen in Figure 3-13. 2.5-5° of external (ER) or internal rotation (IR) were introduced via custom angular shims beneath the distal femur to adjust this angle to horizontal prior to mechanical load application and maximize the moment arm of the femoral neck.

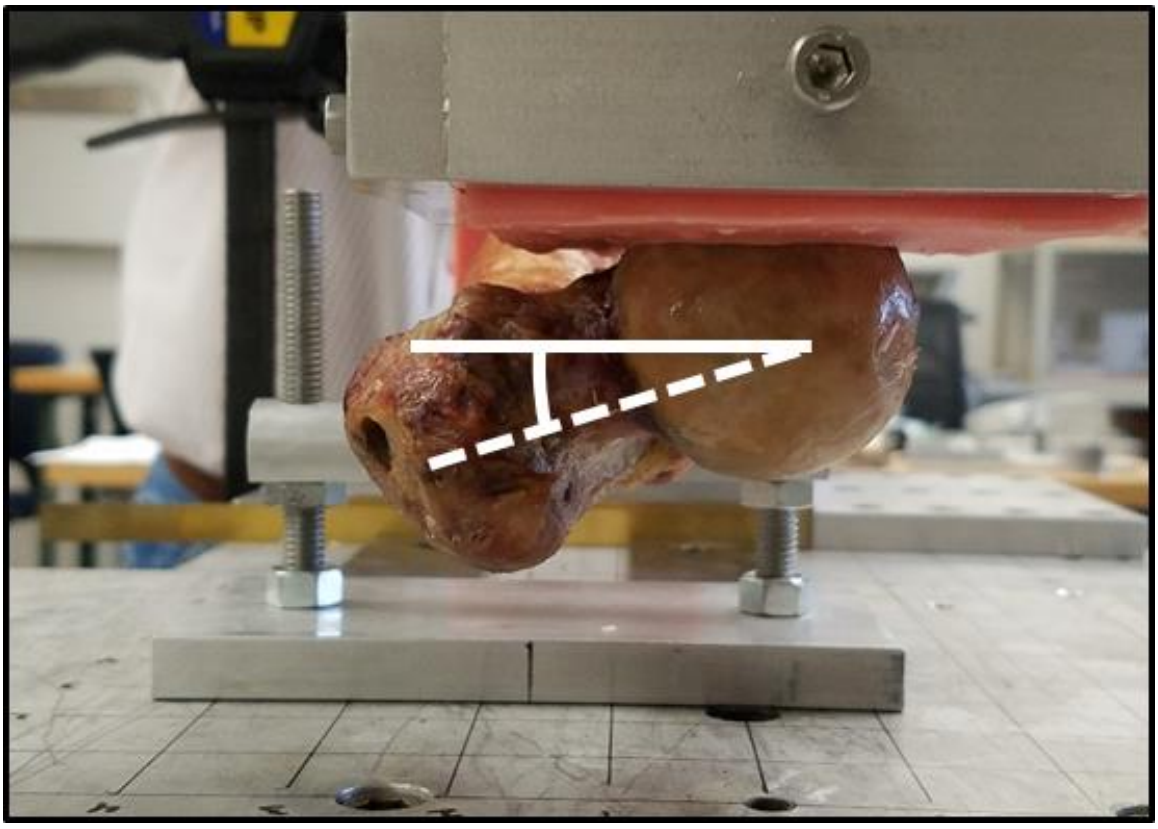

Figure 3-13 Femoral neck within test set-up before rotational (IR) adjustment. A significant angular correction was necessary to maximize the moment arm and make the neck horizontal.

Next, a cylindrical support was placed beneath the femur approximately 114 mm from the center of the femoral head perpendicular to the long axis of the bone. This adjustable support was set at a height to contact the bone but not raise the specimen. This support restricted whole femur bending, but allowed in-plane translations and all rotations. Finally, the center of the femoral head was placed beneath the testing system crosshead for application of load. The off-set nature of the load from the long-bone axis created a moment about the shaft in which the femoral neck acted as the moment arm [47-49, 51]. A schematic of this testing set-up can be seen in Figures 3-14 through 3-16. Testing was performed on an MTS Bionix 858 Test System (MTS Systems Corporation). All MTS manipulation was performed by a Dell PC, with an Intel Core 2 vPro processor, running on Windows Vista.

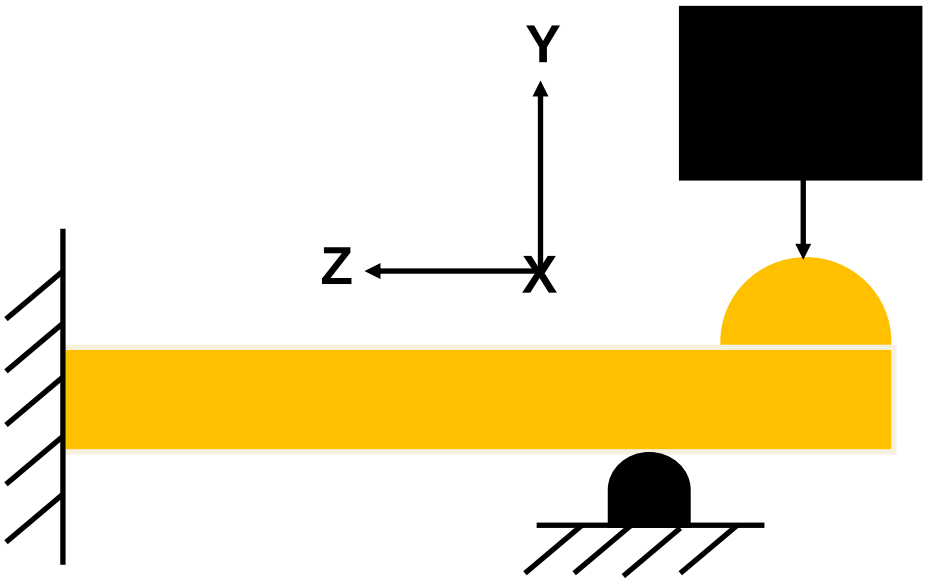

Figure 3-14 Off-set torsional test schematic as viewed from the lateral side of the femur. The distal end of the specimen was assumed fixed by the PMMA block, the roller support beneath resisted translation in the negative y-direction, while the load was applied in the negative y-direction via MTS crosshead to the center of the femoral head. Thus, a torsional moment in the positive z-direction about the femoral shaft is created during loading.

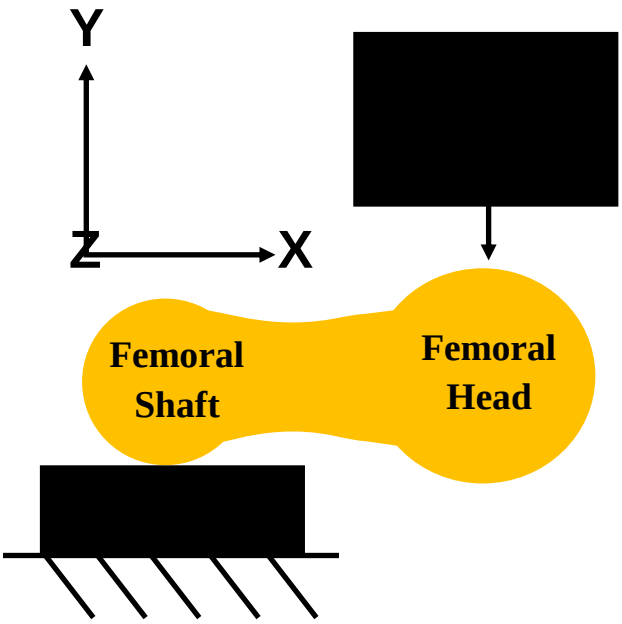

Figure 3-15 Off-set torsional test schematic as viewed from the proximal side of the femur. Vertical load was applied directly to the center of the femoral head via MTS crosshead.

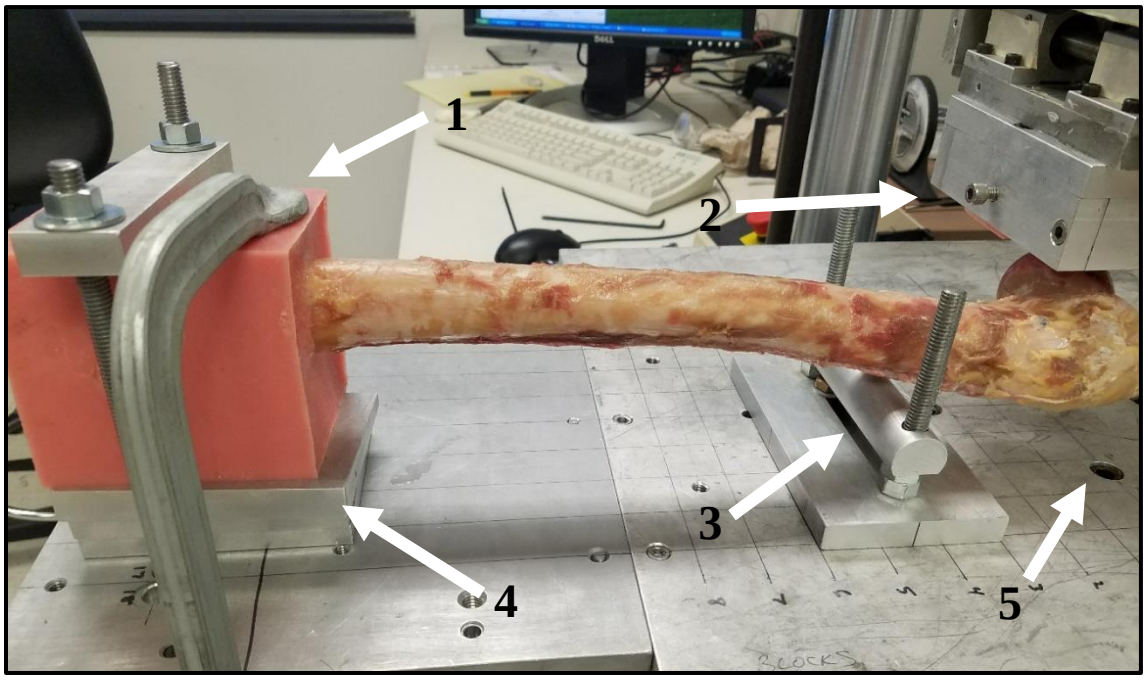

Figure 3-16 Specimen test set-up. 1 = The clamped distal portion of the femur, 2 = The MTS crosshead applying load to the femoral head, 3 = The roller support which can be raised or lowered until just contacting the femoral shaft, 4 = The metal plates and shim placed below the clamped distal femur to adjust the height and orientation of the specimen, 5 = The load cell, aligned co-linearly with the axis of loading, beneath the testing surface.

3.4 Loading Paradigm

Once a specimen was oriented correctly within the test set-up, a 50 N pre-load was applied to the femoral head via the head cast, and the displacement and load measured by the MTS were zeroed. Next, 2 mm of displacement were applied at a rate of 0.1 mm/sec and removed, a total of three times. The specimen was inspected for signs of failure between each test. These tests pre-conditioned the specimen and ensured the femur behaved normally during repeated, low-displacement, loads. For the load-to-failure experiment, displacement was applied at a rate of 0.1 mm/sec until catastrophic specimen failure occurred. An illustration of this loading paradigm is shown in Figure 3-17 [47-49, 51]. Specimens were preserved with saline solution throughout this process.

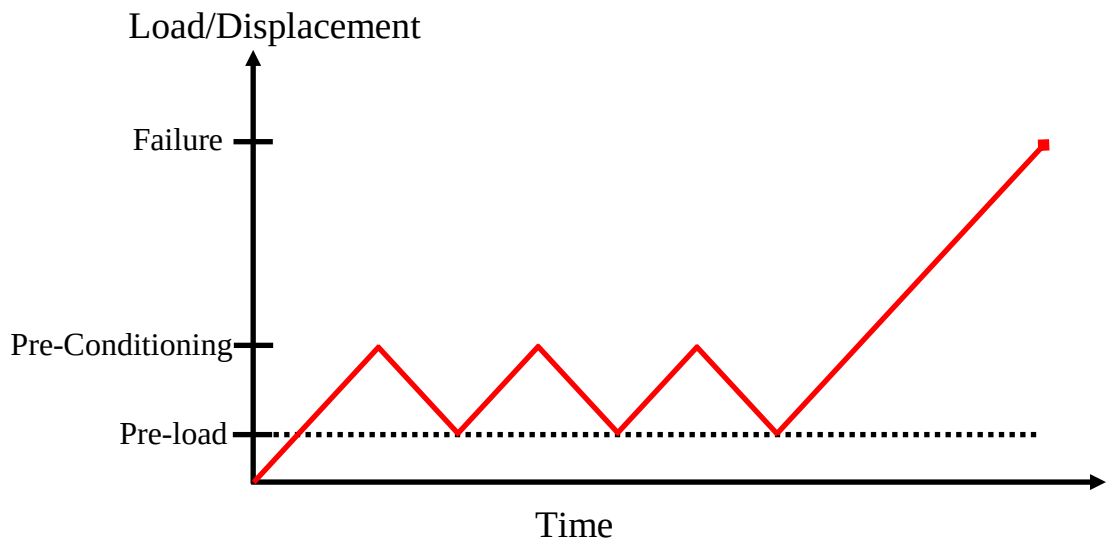

Figure 3-17 The loading paradigm applied to each specimen. The dashed line at pre-load represents the new zero for both force and displacement.

3.4 Data Collection

Force was measured via load cell mounted under the testing set-up. Throughout testing, force and displacement were recorded by the computer work station. The location and height of the roller support and base fixture were measured via ruler and documented. Additionally, the location and extent of each fracture was documented and imaged. After fracture, individual fracture pieces were zip-tied back together for transportation to the CT scanner for post-fracture images of each specimen. Scanning parameters were similar to those obtained post-lesion creation. These CT images permitted visualization of all specimen fracture lines. The dimensions of each femoral head cast were measured via ruler to determine loaded surface area.

CHAPTER 4: CREATION AND VALIDATION OF SUBJECT-SPECIFIC FINITE ELEMENT MODEL

4.1 Geometric Model Creation

4.1.1 Computed Tomography Segmentations

The initial step in generating FEA models was the creation of specimen-specific geometries. First, the CT scan of each specimen after initial lesion creation was imported into Seg3D (Center for Integrative Biomedical Computing, University of Utah), a software program capable of manipulating a CT image series in the axial, coronal, and sagittal planes. An automatic, logarithmic, thresholding algorithm was run on the CT images, separating low-intensity pixels from high. Pixels below the threshold were identified as areas of low-intensity: the air surrounding the specimen, the specimen wrapping, and areas of low density including the lesion, intermedullary canal, and porous trabeculae. Pixels above the threshold were identified as locations of high intensity: the cortical bone and relatively high-density trabeculae. The high-intensity pixel locations, or segmentations, were exported to Matlab (MathWorks, Natick, Massachusetts) as binary image stacks. The thresholding process can be seen in Figure 4-1. Within Seg3D, a 3D geometric shell called an isosurface was generated from the set of high-intensity pixels and exported as an ASCII stereolithography (STL) file. This isosurface encompassed all segmented surfaces including the exterior of the bone, the surface surrounding the lesion, and surfaces surrounding the intermedullary canal.

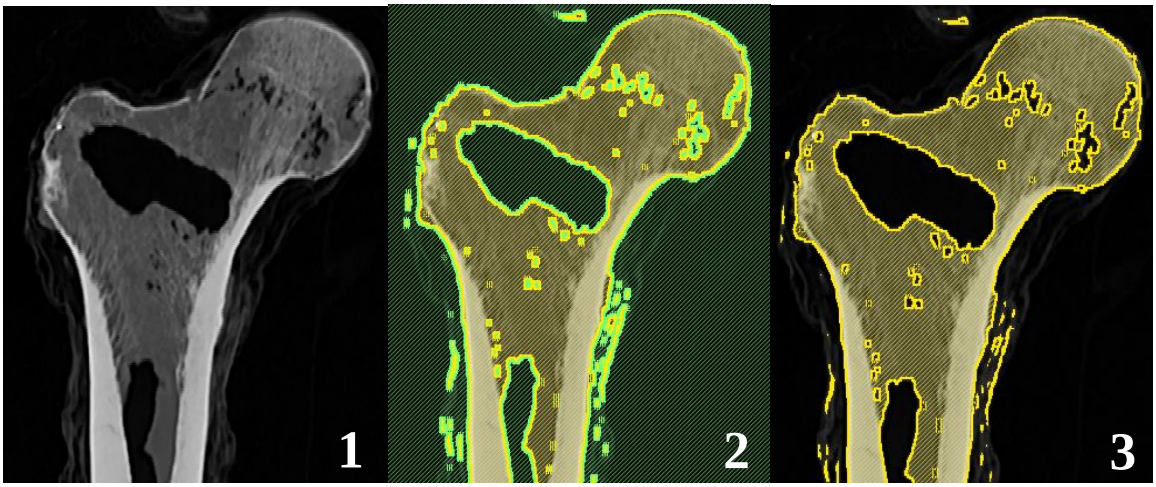

Figure 4-1 Varying stages of the automatic segmentation process. The unaltered, coronal CT slice can be seen in Image 1. The thresholded CT, with green pixels representing low intensity and yellow representing high, can be seen in Image 2. The final set of high intensity pixels, or segmentations, of interest can be seen in Image 3.

4.1.2 Geometric Refinement and Orientation

Each specimen's isosurface was imported into Geomagic Studio (3D Systems, Rock Hill, South Carolina) and visualized as a triangulated surface mesh. To reduce the number of nodes and elements in the final mesh and ease the computational burden when running each FE model, the distal PMMA block portion of the isosurface was deleted. Next, small, extraneous surfaces, generated due to portions of specimen wrapping being included in the segmentation (Figure 4-2), were deleted. Additionally, due to the automated segmentations of the intermedullary (IM) canal and lesion space, separate surface information generated inside the external whole-bone surface was deleted. The resulting triangulated surface mesh consisted of superficial bone geometry only. This surface generation and simplification process can be seen in Figure 4-2.

Figure 4-2 Stages of the geometric cleaning process. From left to right: rough 3D surface with the distal block, rough 3D surface without the distal block, and cleaned 3D surface. The extraneous surfaces are highlighted with black arrows.

The resulting surface geometry was refined with a global, target triangular edge length of 3 mm. During the FE meshing process, surface refinement directly influences mesh density. Therefore, the surface mesh was further refined into three distinct sections, based on the level of mesh density required for adequate FEA. The distal 10 to 14 cm of bone, depending on femur size, was kept at a target edge length of 3 mm. This coarse surface mesh density was thought to be acceptable as this section of the specimen was not directly loaded or contacted during testing. The next 10 to 14 cm of bone, depending on femur size, was refined to a target edge length of 2 mm. The length of this refinement region was chosen to fully encompass the roller support by 4-7 cm on each side, and the refinement was necessary due to the contact interaction with the roller support. Finally, the remaining proximal portion, from the lesser trochanter to the femoral head, was refined to a target edge length of 1 mm, as seen in Figure 4-3, to fully capture the effects of the simulated lesions.

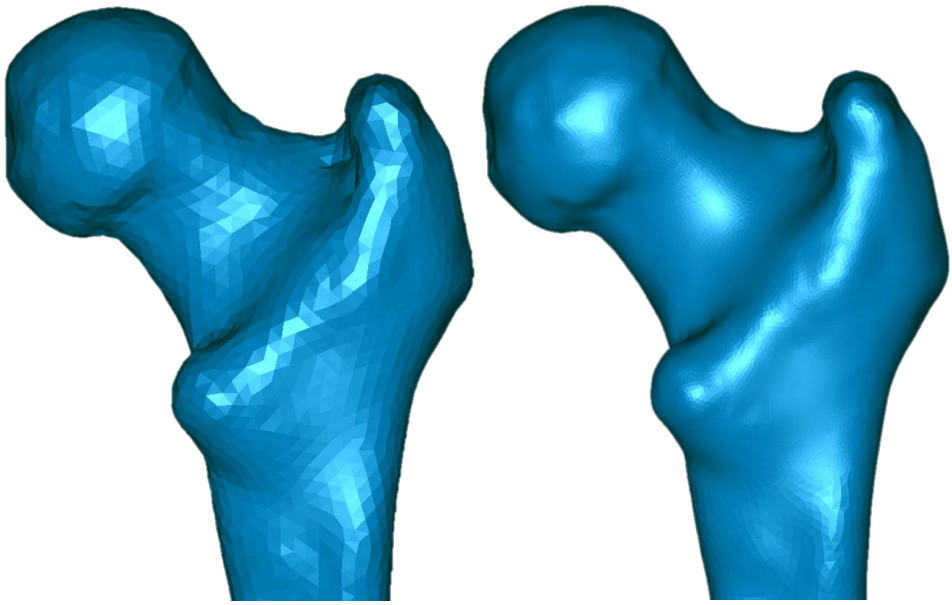

Figure 4-3 Proximal femoral surface meshes before (left) and after (right) refinement. Surface triangulation is far more difficult to visualize after refinement and the refined surface more accurately approximates specimen geometry.

4.1.3 Convergence Study

For verification of adequate mesh density in the proximal region, a convergence study was performed. Models were created with increasing proximal mesh densities by refining target edge length to 4, 3, 2, 1, 0.75, and 0.5 mm. For each model, the deflection of the anterior surface of the femoral head was determined and compared against the physically measured displacement values. Additionally, the maximum stress in the proximal region of mesh refinement was recorded. Each model's run-time and total number of elements were also noted.

Proximal mesh density converged at a target element edge length of 1 mm, which can be seen in Figure 4-6 and 4-7. Femoral head deflection converged at approximately 110% of measured cadaveric femoral deflection. This was likely due to the linear elastic material assumption made in the FEA models. Bone behavior is naturally non-linear [52], and the inability of a linear FEA model to develop plastic strains would result in a less stiff model which would produce greater deflections than those seen during mechanical testing. Additionally, less dense meshes in the proximal femur possess fewer nodes for load to be distributed over. This simulated individual large loads applied over the femoral head, rather than the distributed loading applied mechanically, which also resulted in much greater deflections. Maximum von Mises stress in the proximal region converged at approximately 36 MPa.

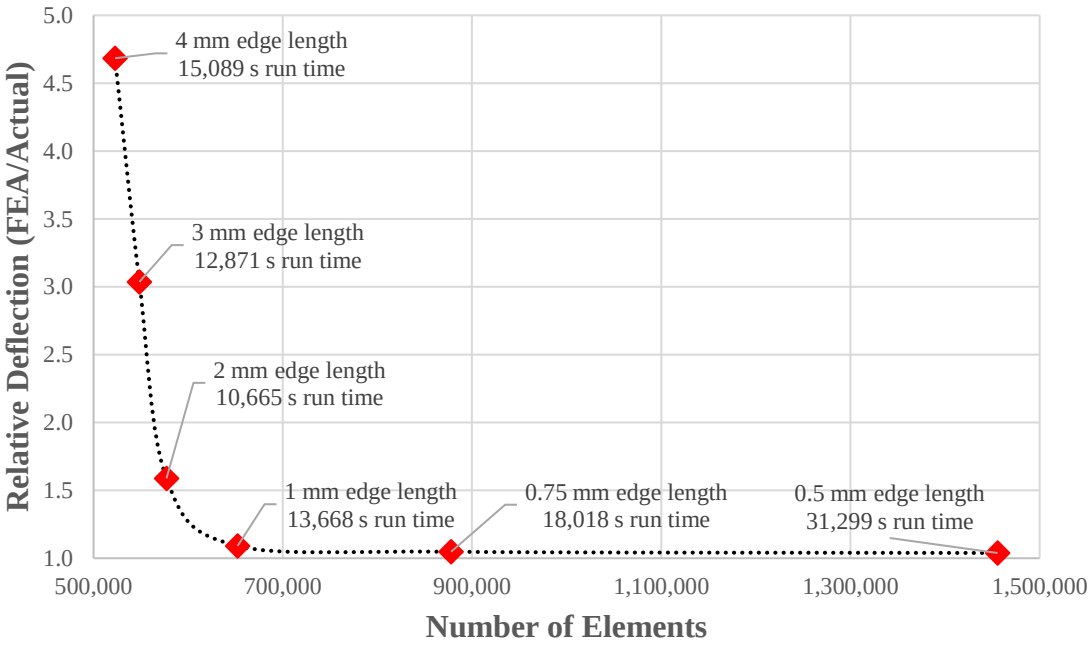

Figure 4-4 FEA displacement convergence study. Coarse proximal meshes experienced deflections three to five times that of actual. Additionally, although proximal meshes with target edge lengths of 0.75 mm and 0.5 mm marginally improved calculated deflection values, they also required 1.5-3x the runtime, respectively, of the 1 mm model.

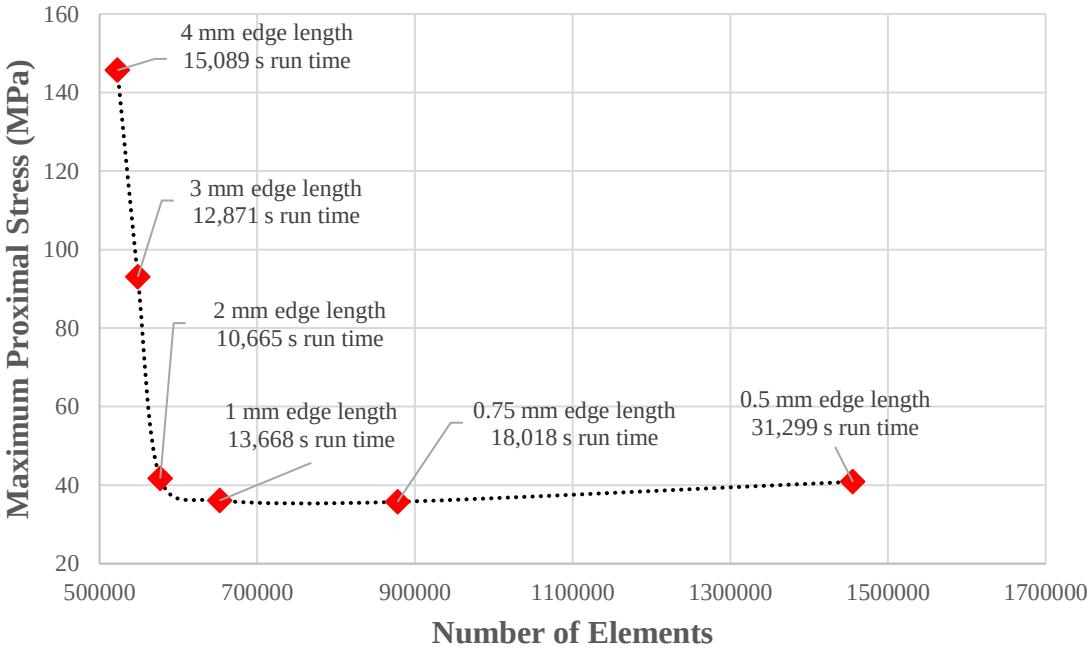

Figure 4-5 FEA von Mises stress convergence study. Artificially high stresses in the coarse proximal meshes were likely also caused by large individual loads being applied as opposed to a distributed loading.

4.1.4 Geometric Orientation

Once refined, the surface model was aligned to the Bergmann coordinate system by matching it to a template femur (from the NIH Visible Female) [42, 53] already positioned in that coordinate system based on bony landmarks, as seen in Figure 4-4. In this standardized orientation, load vectors could be uniformly defined for all models. The aligned surface model was exported as an ASCII STL file for meshing. The transformation matrix between the original surface orientation that resulted from position of the specimen within the CT scanner and the surface oriented in the Bergmann coordinate system was saved for later application during material property assignment.

Figure 4-6 The specimen surface model (red) aligned to the visible female femur pre-aligned in the Bergmann coordinate system (blue). Alignment was performed by selecting three or more points of coincidence and then running an iterative closest point algorithm to bring the surfaces into agreement.

4.2 Finite Element Model Definitions

4.2.1 Element Selection

Element type was an important decision when creating the FEA meshes in this work. Although hexahedral meshes are more computationally robust, especially in contact situations, they also require manual meshing techniques for complex geometry. Tetrahedral meshes, however, can be quickly and automatically generated, often using open-source software, for any manifold, or non-self-intersecting geometry. As minimal contact was modeled in these FEA models, and with the goal of one day providing fracture assessment in a clinical setting, linear, tetrahedral meshes were chosen for this work.

4.2.2 Mesh Creation

The software program TetGen (Weierstrass Institute for Applied Analysis and Stochastics, Berlin, Germany) received the STL surface mesh exported from Geomagic Studio and generated Delaunay tetrahedral meshes as an output. TetGen was run via command prompt window using the following command "tetgen -pYq1.2Va1 [surfacemesh].stl". Several parameters were input to affect mesh quality: -p instructed TetGen to import boundary information from the STL file, -Y constrained the mesh to the existing surface triangulations, -q1.2 specified a maximum radius-edge ratio of 1.2, -V gave the user mesh quality statistics, and -a1 specified a maximum tetrahedral volume of 1 mm^3. The resulting mesh was evaluated visually via the accompanying software, TetView (Figure 4-5). Next, using Matlab, rotations corresponding to the IR/ER correction applied during mechanical testing to account for femoral neck angle (Figure 3-14) were applied to the nodal coordinate information of each mesh. Each model

orientation then matched the corresponding specimen orientation during mechanical testing. The oriented node and element information were exported as an Abaqus input deck for use in the analysis.

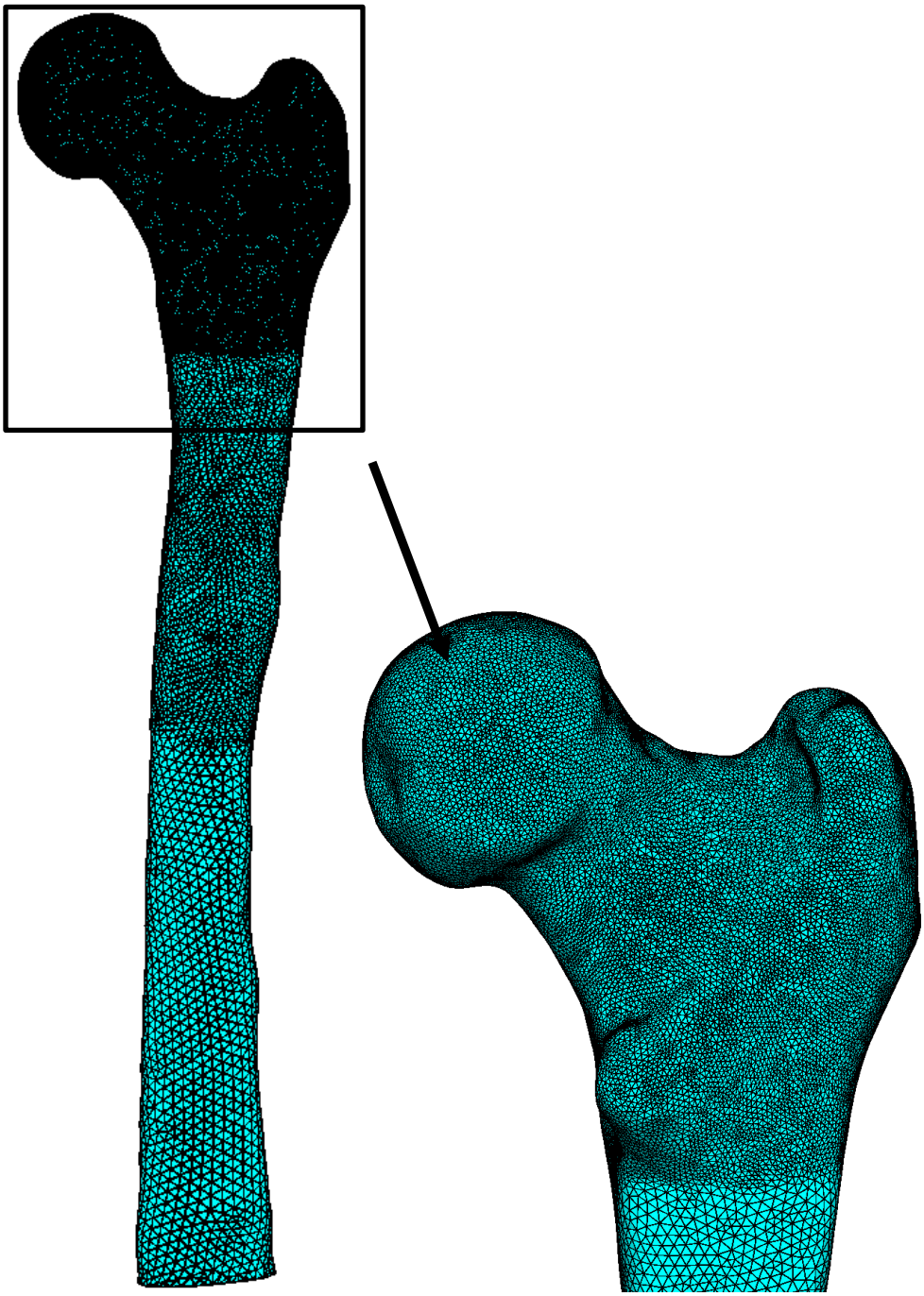

Figure 4-7 Representative specimen tetrahedral mesh. The areas of low, medium, and high mesh density can be clearly seen.

4.2.3 Material Properties

As a diagnostic imaging modality, CT provides bone density information in the form of intensities. In CT images, denser bone will appear white, while less dense bone will appear darker (grey or black). Utilizing these intensities, element material definitions were applied. All calculations were performed in Matlab. First, the CT images were imported, and the pertinent digital imaging and communications in medicine (DICOM) information was extracted from the header information. These data included the intensity values for each image pixel, the relative location of each axial CT slice, the pixel size, and the specimen offset during scanning. These data were filtered by the binary image stacks exported from Seg3D so that all pixel intensities below the applied segmentation threshold (Figure 4-1) were set to zero. Next, the FE mesh information needed to be related back to the CT space to determine element intensity values. Element centroids were calculated from the node and element files generated by TetGen, and the transformation file calculated during alignment to the Bergmann coordinate system was utilized to determine locations of element centroids within the CT space. Voxel intensities in a 1 mm sphere around each centroid were averaged to calculate each element's centroidal, CT intensity value [54].

Element intensities were transformed into elastic moduli and yield strength values using several established relationships. First, element intensities were converted into Hounsfield units (HU) through a linear relationship specified in the DICOM header data. CT-based densities were derived from element HU: CT density = 0.7502*HU – 17.1088. These were then converted into ash-based, mineral densities: ash density = 0.694*CT density +111 [55]. Ash densities were divided by 1000 to yield units of g/cm^3. From

these ash-based densities, each element's elastic modulus was calculated. If ash density was less than 0.27 g/cm^3, the following relation was used: elastic modulus = 33,900*ash density$^{2.2}$. If ash density was greater than 0.27 g/cm^3 and less than 0.6 g/cm^3, the following relation was used: elastic modulus =5,307*ash density +496. Finally, if ash density was greater than 0.6 g/cm^3, the following relation was used: elastic modulus = 10,200*ash density$^{2.01}$ [56].

Due to mesh sizes on the order of hundreds of thousands of elements, elemental material properties were grouped into 100 sets of averaged modulus values to reduce computational burden. All elements with intensity values of 0, which were those within the lesion or in the intramedullary canal, were assigned an elastic modulus of 0.01 and assumed to have yielded during analysis [35]. A constant Poisson's ratio of 0.4 was assumed [57]. Grouped elastic moduli element sets and their corresponding elastic moduli were written to Abaqus input decks for FEA.

Element yield strengths were similarly calculated from image intensity-based density information. If ash density was less than 0.317 g/cm^3 the following relation was used: yield strength = 137*ash density$^{1.88}$. If ash density was greater than 0.317 g/cm^3, the following relation was used: yield strength = 114*ash density$^{1.72}$ [35]. In contrast to the assignment of elastic modulus, each element was assigned an individualized yield stress value. These values were written to a text file for use in post-processing.

4.2.4 Boundary Conditions

Boundary conditions (BCs) were assigned to mimic the applied mechanical testing conditions as closely as possible. The clamped region of the specimen was replicated by restricting the displacements of each node in the distal 5 mm of the model to zero. The roller support interaction was modeled by creating a rigid analytical surface (RAS) of the same size and shape as the physical roller support device (22 mm diameter cylinder). A reference node at the center of the cylinder, associated with the RAS, constrained displacement of that surface in all directions. The RAS was placed directly beneath the model such that the two objects would come into contact during the first increment of load application. In Matlab, surface element sets comprising approximately 45 mm of the model surrounding the RAS were created, and no-slip, frictional contact between these element sets and the RAS was defined with a coefficient of friction of 0.6 [58]. For analysis purposes, the RAS was specified as the master surface and the surface element sets as the slave. These BCs can be seen in Figure 4-8.

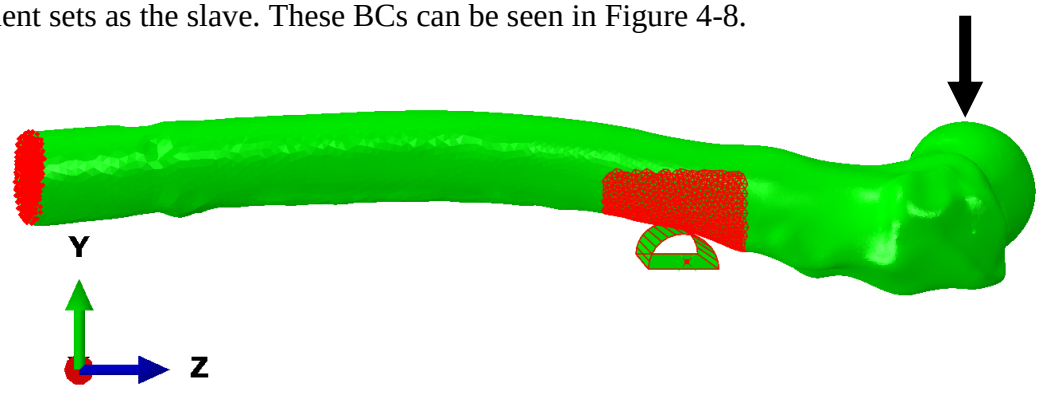

Figure 4-8 Model boundary conditions. The fixed node set mimicking the clamped, PMMA block can be seen on the left. The surface element set defined for contact with the roller support can be seen on the right. The model coordinate system is also visualized with the y-axis representing the anterior-posterior (AP) direction, the z-axis representing the superior-inferior (SI) direction, and the x-axis representing the medial-lateral (ML) direction.

4.2.5 Loading

Loading conditions were also defined to mimic the load application used during mechanical testing as closely as possible. All surface nodes comprising the femoral head were identified by fitting a sphere to the geometry of the head, and a load vector in the negative y-direction was defined as seen in Figure 4-6. This load vector corresponded to the MTS-applied vertical load. Geometric information from the PMMA head cast that was measured after testing was utilized to determine the subset of nodes to which load should be applied to simulate the mechanical test. The recorded maximum force during mechanical testing was distributed uniformly across the node subset [59]. Additionally, to account for possible zero intensity surface elements that may have been included in the loaded node set, all elements with loaded nodes were assigned a uniform modulus value equal to median within the set.

4.3 Analysis Methods

All FEA was performed using Abaqus/Standard (v. 6.17; Dassault Systèmes, Velizy-Villacoublay, France). Abaqus/Standard utilizes a Newton method solver which implicitly calculates nodal displacements at each time step. However, due to the initial contact between the model and RAS, early models failed to achieve Newton solver convergence in a single time step. To compensate, step increment size was restricted to one hundredth of a time step, yielding 100 total increments and simulating the slow application of load seen in mechanical testing.

4.3.1 Failure Assessment

The relevant FEA model output was chosen based upon two main criteria: relevance to a clinical setting and ability to predict fracture during later analysis. The maximum principle strain theory applies a binary yield strain value to each element based upon the element's compressive or tensile, maximum strain. Failure is assumed when element strain exceeds yield strain [60]. Similarly, the von Mises stress theory assumes failure when an element's von Mises stress exceeds an element's yield stress [56, 61]. Both the maximum principle strain and von Mises failure theories have been proven as adequate predictors of fracture in the proximal femur during varying loading situations [62]. However, while von Mises can utilize element yield stresses calculated from CT intensities, maximum principle strain theory assumes healthy bone behavior for yield values. Clinically, patients suffering from metastatic disease possess bone biology significantly different from that of normal bone. For this reason, the von Mises stress theory was chosen.

The method of predicting fracture location was described in Section 2.1.3. Contiguous failed element sets were determined and their total volumes calculated. Contiguous element sets of $\geq$30 mm^3 were deemed likely locations of fracture. This threshold was lowered from the critical volume used in previous work to ensure the capture of all possible locations of fracture. These failed element sets were written to text files, imported into Abaqus, and visually compared with fracture lines. Successful prediction of fracture was defined as a contiguous failed element set in the location of mechanical fracture. Elements with intensity values of zero were assumed to have yielded prior to loading and were excluded from this analysis.

CHAPTER 5: RESULTS AND DISCUSSION

5.1 Mechanical Fracture Locations

All data collected during mechanical testing, including the total applied load, total applied deflection, and other relevant measurements, are shown in Table 5-1. Most specimens experienced similar total applied loads and deflections.

Table 5-1 Mechanical Testing Recordings and Measurements

Specimen Identifier	Total Load (N)	Total Deflection (mm)	Distance of Roller Support to Femoral Head (mm)	Femoral Head Loaded Area (mm^2)
Large Blowout	1277	12.7	114	528
Small Blowout	2302	16.7	114	1018
Combination	918	7.3	102	1257
Tortuous	1063	13	114	424
Lateral	1544	12	114	855

Of the five cadaveric specimens, four fractured through the simulated lesion. Only the tortuous specimen fractured in a manner that did not involve the lesion, with a spiral pattern further down the shaft (Figure 5-1). It is likely this specimen experienced a spiral-type fracture, rather than a trochanteric fracture, due to the relatively intact medial cortical bone that remained in the femoral neck with this lesion pattern. This region's ability to fully bear load appears to have allowed a purer torque to be applied to the long axis of the bone, resulting in a spiral-type fracture. This specimen also possessed somewhat atypical bone structure as seen in Figure 5-2.

In addition to failure through the lesion, the specimen with the combination lesion experienced large amounts of bone failure at the roller support. This phenomenon was recorded in other specimens, but to a much lesser extent. As this specimen's donor

suffered from amyotrophic lateral sclerosis (ALS), a disease which affects muscle and bone strength [63], this non-lesion failure is attributed to poor bone quality. Fracture locations in the large blowout, small blowout, combination, and lateral can be seen in Figures 5-3, 5-4, 5-5, and 5-6, respectively.

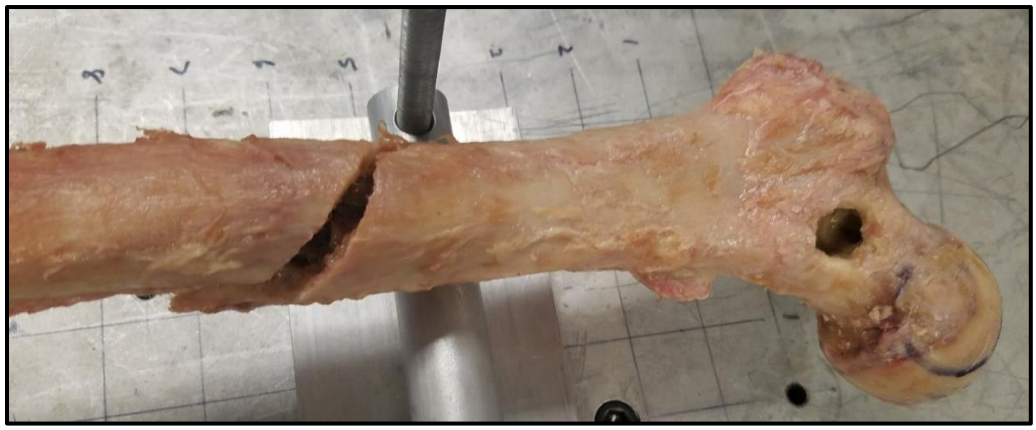

Figure 5-1 The spiral fracture that occurred in the specimen with the tortuous lesion. Prior to testing, it was noted that this particular specimen possessed atypical bone structure with very pronounced trabeculae, as seen in Figure 5-2.

Figure 5-2 Coronal CT slice of the cadaveric specimen in which the tortuous lesion was created. Atypical features include thicker cortical bone in the femoral neck and a denser, more heterogenous, trabecular structure.

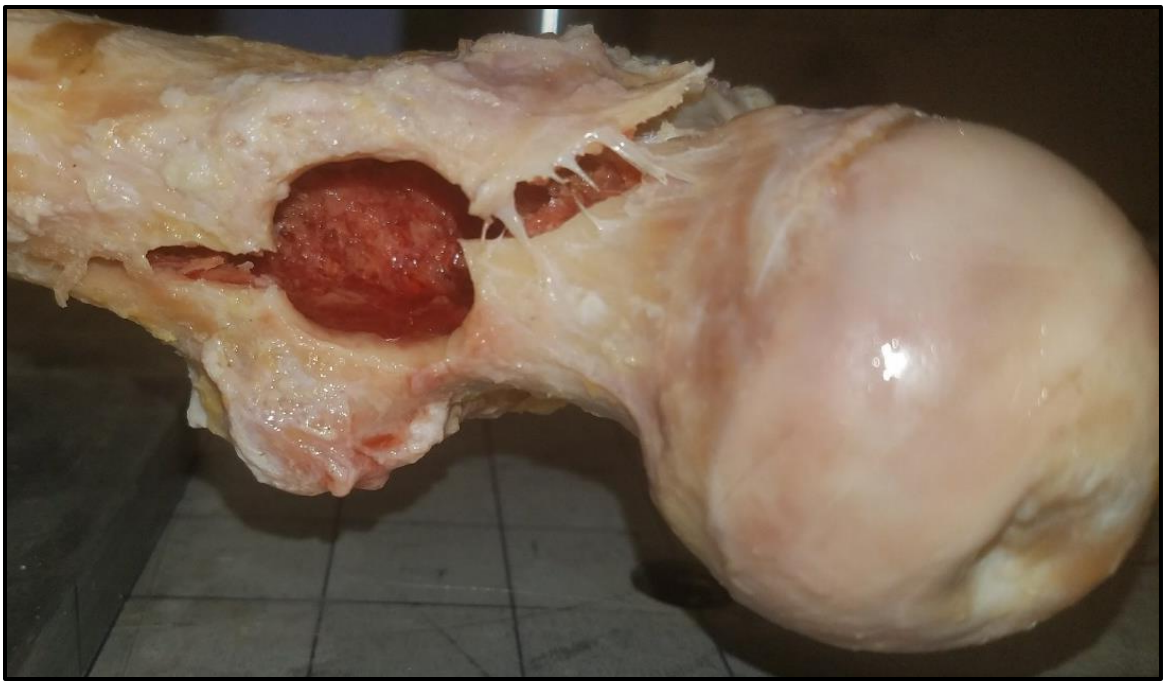

Figure 5-3 Fracture location in the specimen with the large blowout lesion as viewed from the medial side. The fracture line ran through the intertrochanteric region, directly through the lesion site.

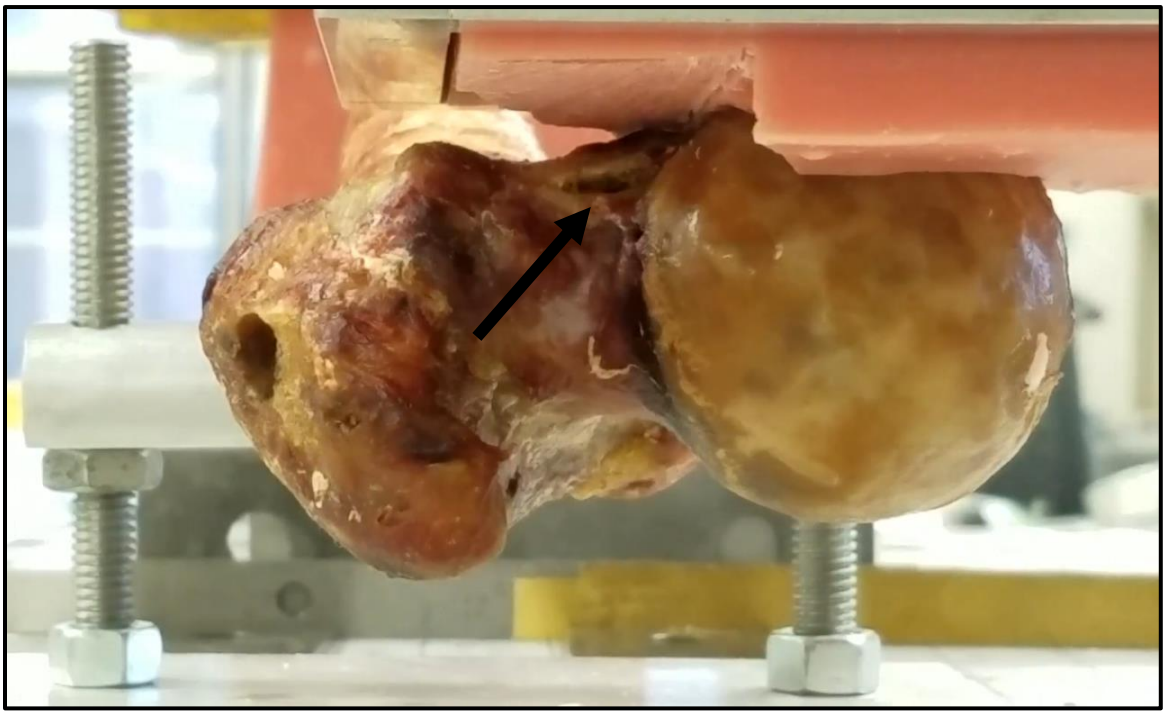

Figure 5-4 Fracture location in the specimen with the combination lesion as viewed from the proximal side. Fracture occurred in the anterior femoral neck and propagated distally through the lesser trochanter.

Figure 5-5 Fracture location in the specimen with the lateral lesion as viewed from the medial side. The fracture line ran subcapitally and to the lesser trochanter, nearly removing the entire femoral head.

Figure 5-6 Fracture location in the specimen with the small blowout lesion as viewed from the medial side. The fracture line ran through the greater trochanter and extended through the intertrochanteric region, into the femoral shaft.

5.2 Finite Element Analysis Fracture Location Prediction

FEA was able to predict fracture locations in all five specimens. In general, failed element set volumes that corresponded to physical fractures were larger than 30 mm^3. With the exception of the combination lesion, all failed element sets in the areas of cadaveric fracture were greater than 100 mm^3. Paired FEA and mechanical fracture locations in all specimens are shown in Figures 5-7 and 5-8.

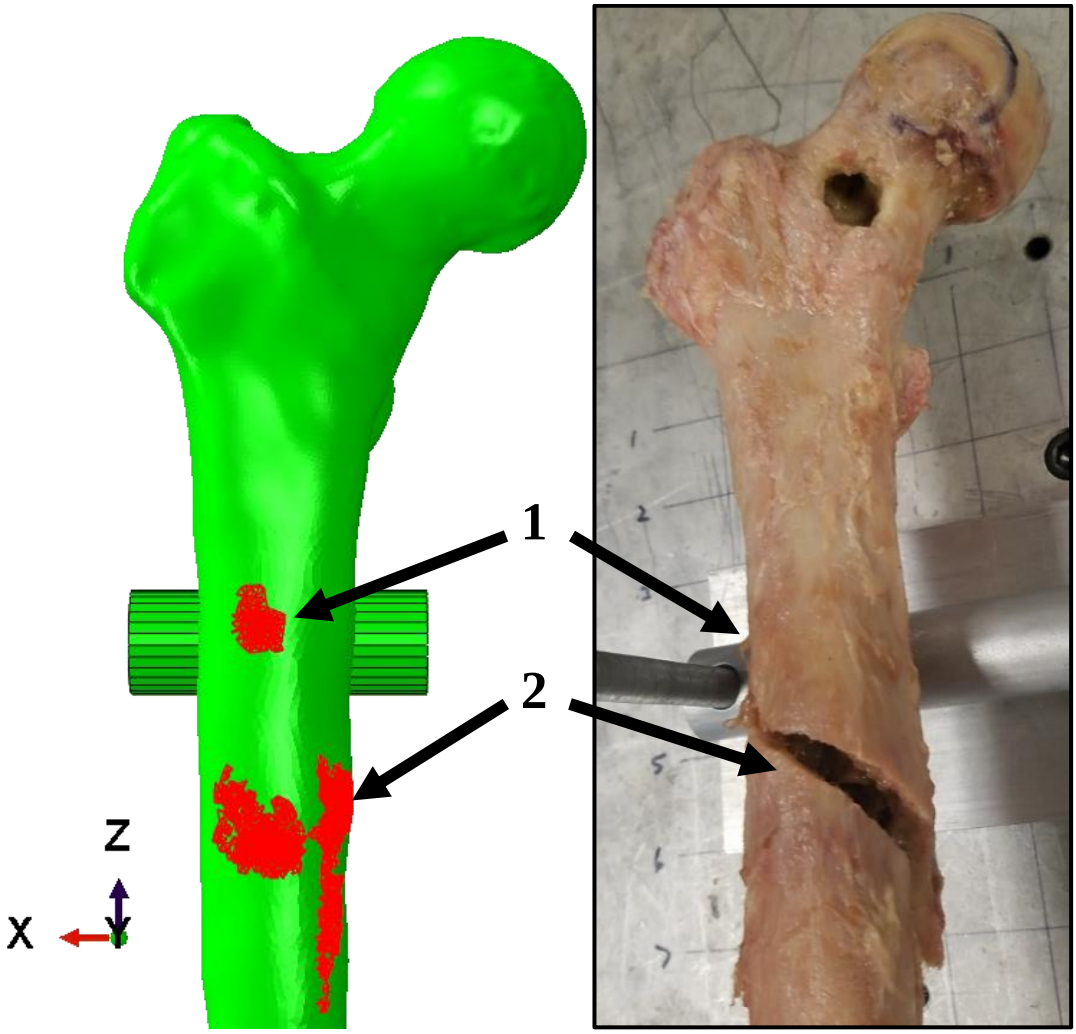

Figure 5-7 FEA (left) and cadaveric (right) fracture locations in the tortuous lesion. 1 = Bone failure at the point of contact with the roller support. 2 = Bone failure in the cortical shell at the posterior and medial sides.

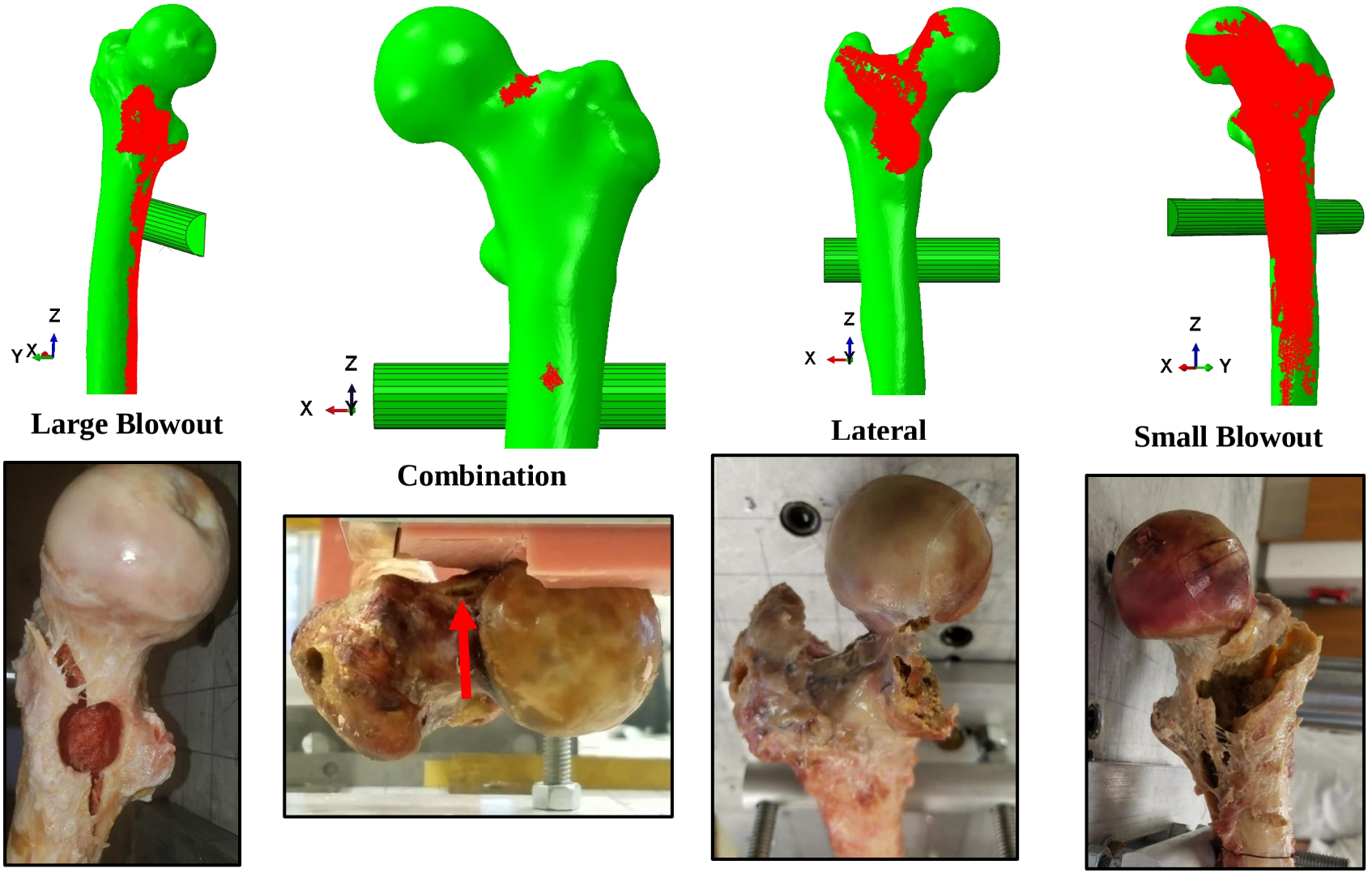

Figure 5-8 Fracture locations in FEA and cadaveric femora

In all models, sets of failed elements in the trabeculae surrounding the IM canal were found, although this failure could not be documented during testing or on CT images given that CT resolution was not small enough to distinguish individual trabeculae. In the large blowout lesion, FEA predicted fracture correctly around the lesion shape, though with slightly more distal propagation and slightly less proximal propagation than was seen cadaverically. Fracture was also falsely predicted in the subcapital neck and head region, attributable to partial volume effects that resulted from surface smoothing. In the combination lesion, two smaller failed element sets of 32 mm^3 and 40 mm^3 were found at the roller support and in the area of cadaveric fracture, respectively. As the combination lesion fracture developed the smallest fracture line and fractured the least destructively this makes it likely this specimen would have smaller failed element sets. In the lateral lesion, fracture was accurately predicted in the femoral neck region and along the lesion shape. However, nearby, failed element sets also extended proximally into the head and distally into cortical bone of the shaft where fractures did not occur. These locations were attributed to the static FE analysis preventing release of fracture energy. Finally, in the small blowout specimen, a relatively large failed element set was found in the location of fracture extending from the femoral head to the distal shaft. This element set likely encompassed more than the fracture area due to static analysis methods. As in the specimen with the lateral lesion, these additional locations of predicted fracture were likely caused by the prevention of release of fracture energy. No other failed element sets were found.

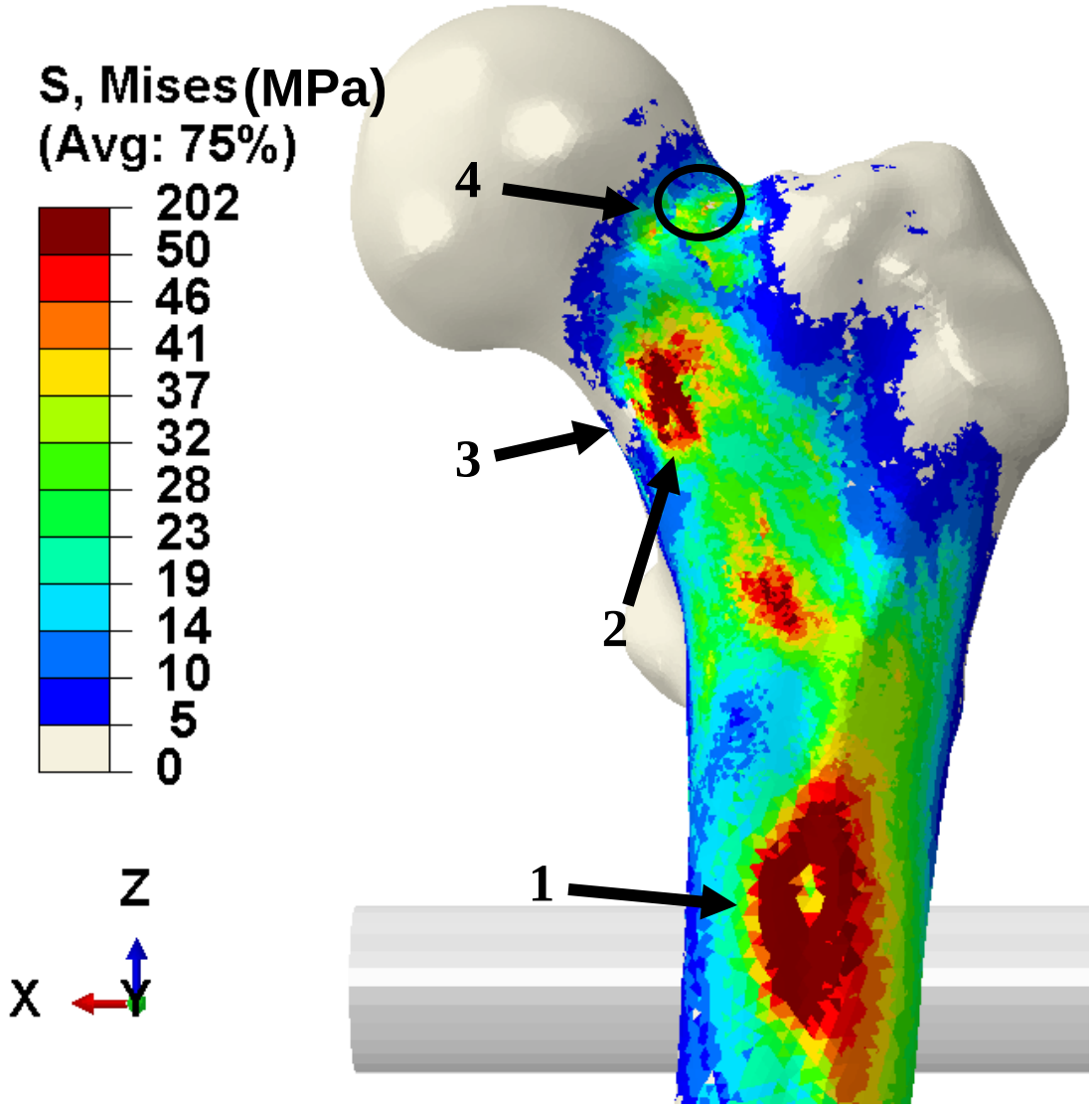

Figure 5-9 FEA von Mises stress contours of the specimen with the combination lesion during off-set torsion testing. 1 = Large stresses are seen in the cortical bone bending over the roller support. 2 = Large stresses are seen proximally and anteriorly from the lesion site in the femoral neck. 3 = Location of lesion cortical involvement. 4 = Location of cadaveric fracture.

Although FEA was able to predict mechanical fracture location, sets of failed elements which were indicative of fracture were also found at other locations. For example, in the tortuous lesion, failure was correctly predicted at the roller support and in the cortical shell where spiral fracture occurred (Figure 5-8). But, fracture locations were also predicted to occur at certain bone surfaces, in the femoral head, and in the trabeculae in the distal shaft (Figure 5-10).

There are several potential causes of these additional locations of predicted fracture. First, the static application of load in our modeling approach inhibited elements from yielding dynamically during analysis. In the models, elements with stresses greater than their yield stress continued to carry load despite their exceeding yield which, in physical reality, would have resulted in a crack. Our FEA models prevented the release of energy through fracture. Partial volume effects on surface elements may have also introduced error. During the calculation of material properties, it is possible the sphere generated around each element centroid contained air outside the bone. This inclusion could lower the element's centroid averaged intensity value to a point where it is being modeled in a way that is not representative of the true behavior of cortical bone. Finally, it is also possible that applying a large number of material properties interrupted the cortical bone's ability to act as a continuum layer around the trabeculae. Reducing the total number of material properties, particularly for the cortical regions may improve the specificity of this analysis.

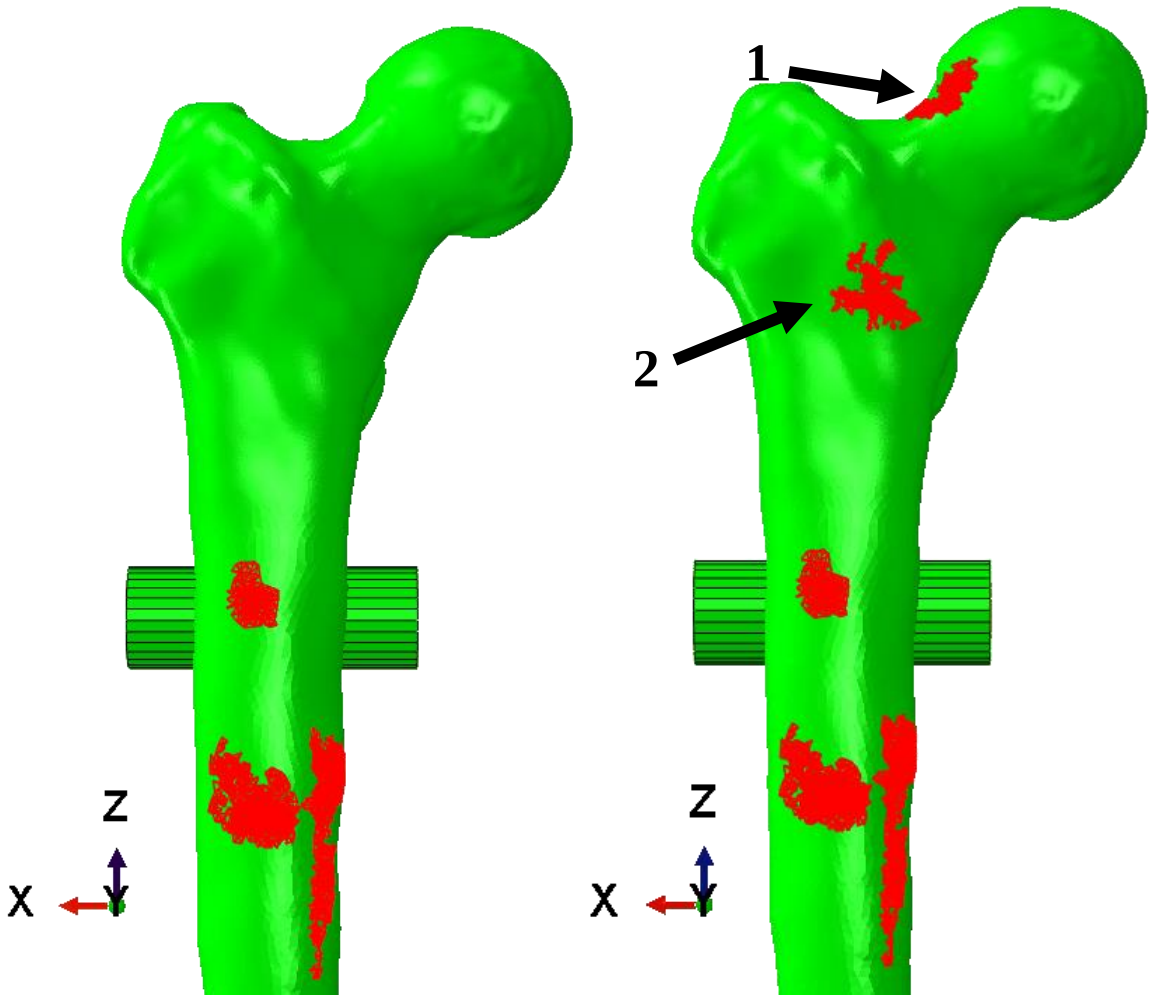

Figure 5-10 FEA failed element sets in the location of fracture (left) and all failed element sets (right) in the tortuous lesion. 1 = Failed element set in the trabeculae of the neck and subcapital head. This artificial failure location is attributed to the static analysis. 2 = Failed element set at the surface of the anterior femur. In general, failed element sets solely at the surface of the bone, with no nearby failed element sets, were assumed artificial failure locations due to partial volume effects.

CHAPTER 6: CONCLUSIONS AND FUTURE WORK

In summary, finite element analysis models were created that were capable of predicting fracture locations in cadaveric femora with simulated metastatic lesions. Several previous studies have analyzed mechanically induced lesions. However, all those defects were ellipsoid or spherical in nature, while clinically encountered lesions are amorphous, tendrilled, chaotic shapes. This is likely due to the metastasis process which, on a cellular level, spreads by removing and replacing bone. Therefore, modeling spherical or ovoid defects holds little relevant value clinically. No research group has produced validated FEA models to study the effects of realistically shaped lesions in femoral bone, whether simulated or actual. The FE models in this work were developed from CT scans of cadaveric specimens with artificially induced metastatic lesions representative of those seen clinically. Models were loaded similarly to the applied mechanical testing conditions. Contiguous element failure was studied in each model and compared to mechanical fracture locations in the physically loaded cadaveric femora. FEA correctly predicted the locations of fracture in five out of five specimens studied.

6.1 Model Limitations

In comparison to many other FE models of the femur, the models utilized in this study were fairly simplified. The long-term goal of this line of work is to implement this analysis technique clinically, alongside Mirels' scoring, which means that it needs to be easy and quick to implement. FEA model complexity could be increased by introducing hexahedral element types or applying load to the models via contact modeling by simulating the head cast. However, these augmentations would require significantly greater model generation and computational time and are not guaranteed to improve

results. Additionally, the transitions between areas of differing mesh densities were very abrupt in these models, which created locations of possible stress concentrations. However, elimination of these possible stress concentrations would require biased meshing techniques in the transition zones which would increase time required for model generation. While for short-term research-only purposes our models could be modified to include more computational complexity, simplified models were emphasized as they would allow for ease of generation and prompt analysis when eventually translated to a clinical setting.

An additional limitation was the analysis of fracture in the model. Theoretically, fracture begins when a crack tip forms in an object under some form of loading. Generally, these crack tips form at stress risers, which is a key reason we attempted to model non-spherical and non-ellipsoidal metastatic lesions that would include such features. As stress in a fracturing object increases, the crack tip extends, or propagates, forming a fracture line. Typically, crack propagation occurs rapidly. In contrast, all analysis in this validation was carried out statically, meaning model element definitions did not change in response to loading to indicate progression of a fracture line through failed elements. A quasi-static analysis technique could be implemented to approximate crack tip formation and propagation behavior in bones suffering from metastatic disease. This could be accomplished by running any given FEA model in small increments until any elements developed stresses indicative of material failure. The elastic moduli of these "failed" elements could then be set to 0.01 MPa, removing their ability to bear further load, and the model restarted from the previous increment. By repeating this process, crack propagation could be partially modeled. To fully model crack propagation, a

separate program, such as the extended finite element method (XFEM) software package in Abaqus, must be used. However, such programs require knowledge of the possible crack domain and the initial crack location, information which is not known a priori, especially in a clinical setting. As such, this software would be impractical for this research. Additionally, fatigue failure, or repeated loading, plays a significant role in the formation of a crack tip. FEA modeling of fatigue failure requires knowledge of material behavior when undergoing permanent, or plastic, strain. However, this information is impossible to determine on a patient-specific basis and thus is also unsuitable for this research.

The model was also limited by a lack of contact interactions for the purposes of loading. Although contact was implemented between the femoral shaft and the roller support, load was distributed across the femoral head through the use of direct application to the surface nodes. By creating a rigid object similar to the PMMA head cast and modeling cartilage on the femoral head, load could be applied more consistently and similarly to that used in mechanical testing. We did not model contact in this validation work for consistency with the previous work detailed in Chapter 2, in which hip joint forces were not modeled through contact with the acetabulum. The assumption of direct loading, rather than contact modeling, affected load distribution over the femoral head during mechanical loading conditions characteristic of activities of daily living. Muscle forces on the femur were also omitted completely. Both omissions could affect internal bony stresses when modeling physiological activities, such as gait. However, these assumptions were thought to be acceptable in this work as the focus of this study was to validate fracture prediction in our models rather than the accuracy of the stress contours.

In terms of mechanical testing, the main limitation was the relatively slow rate of load application. The loading rate used in this work (0.1 mm/s) was a much slower loading rate than that seen during any normal physiological activity such as gait, stair climb, sit-to-stand, or fall [64]. These types of physiological activities are more likely to cause fracture, especially in patients suffering from metastatic disease to the proximal femur. Introducing a higher intensity loading activity with a faster loading rate and then accurately predicting fracture location in FEA would strengthen the validity of our model.

Finally, an automatic segmentation program was used to obtain specimen-specific geometry and material properties. However, this process did not allow the lesion to be separately identified from the bone. Even utilizing manual segmentation, it is difficult to assign true boundaries to metastatic lesions on plain radiographs or in CT images. This is in part due to the mechanisms of metastatic growth in bone. Metastases are initially attracted to areas of bone with high levels of remodeling activity. Subsequently, lesion formation is influenced by whatever the predominant bone remodeling behavior is at that location, either osteoblastic or osteoclastic, but the lesion will ultimately exhibit radiographic traits of both. This is attributed to the mechanism by which blastic lesions grow. Blastic lesions are signaled to initiate bone deposition by bone resorption activities [11]. As such, lesions may appear as bone-like on any imaging modality, with blastic lesions appearing as trabeculae and lytic lesions appearing as spaces between trabeculae. Additionally, the boundary between lesion and bone is at the microscopic level, too small to be resolved on any imaging modality [13]. These factors make it difficult to accurately segment the lesion shape. However, by incorporating the lesion into the model via CT-

based material property definitions, the full impact of the lesion can be assessed without the need to segment its shape.

6.2 Literature Comparison

When comparing this work to that of our peers, similar stress values were found in femoral bone. Maximum stresses found in this work varied between 200-400 MPa while maximum stresses seen in intact, non-lesion, femoral FE models were 64.9 MPa under 500 N of pure bending [65]. Stresses in this study were thought to be best compared to pure bending as it is more representative of the loading seen in off-set torsion. Larger maximum stresses could be expected in our models as our loading was 2-5x higher than 500 N.

6.3 Future Work

Future plans for improving FEA analysis of metastatic disease in the proximal femur include studying additional specimens under the same off-set torsional loading pattern at faster, more physiologic loading rates. This would provide an opportunity to increase our confidence in model validity. Furthermore, studying additional specimens under a separate loading pattern, such as gait, would provide data directly relevant to a physiological activity. Finally, a quasi-static fracture propagation technique could be implemented into the analysis. This could more accurately model fracture behavior and increase specificity when identifying failed element sets, thus improving the diagnostic capability of this analysis.

Clinically, by implementing open source software, the creation of patient-specific FE models may one day be feasible as an assessment technique alongside Mirels'

scoring. Currently, CT segmentation and tetrahedral mesh generation are performed in open source programs, while geometric refinement, model alignment, material property assignment, FEA, and post-processing of results are all performed in commercially available software. Geometric refinement and model alignment could be translated into an open source modeling program most readily. Original code would need to be created to assign material properties and post-process the FEA results. Finally, FEA could be performed in an open source software, such as Code-Aster or ONELAB. Streamlining these processes in open source software would allow for the widespread and timely assessment of fracture likelihood in any patient suffering from metastatic disease. With this additional information, clinicians may have access to a more complete picture of true fracture risk, which should allow them to make more informed decisions regarding patient health – ideally sparing some patients from unnecessary surgery and improving their quality of life.

REFERENCES

1. Singh, S.D., S.J. Henley, and A.B. Ryerson, *Surveillance for Cancer Incidence and Mortality - United States, 2013.* MMWR Surveill Summ, 2017. **66**(4): p. 1-36.

2. Johnson, N.B., et al., *CDC National Health Report: leading causes of morbidity and mortality and associated behavioral risk and protective factors--United States, 2005-2013.* MMWR Suppl, 2014. **63**(4): p. 3-27.

3. Cooper, G.M., *The Development and Causes of Cancer*, in *The Cell: A Molecular Approach*. 2000, Sinauer Associates: Sunderland, MA.

4. National Cancer Institute. *Cancer Staging*. 2015 March 9, 2015 [cited 2018 1-25-18]; Available from: https://www.cancer.gov/about-cancer/diagnosis-staging/staging.

5. Kakhki, V.R., et al., *Pattern and distribution of bone metastases in common malignant tumors.* Nucl Med Rev Cent East Eur, 2013. **16**(2): p. 66-9.

6. Robinson, J.R., et al., *Stage IV colorectal cancer primary site and patterns of distant metastasis.* Cancer Epidemiol, 2017. **48**: p. 92-95.

7. Hosono, N., et al., *Orthopaedic management of spinal metastases.* Clin Orthop Relat Res, 1995(312): p. 148-59.

8. Boland, P.J., J.M. Lane, and N. Sundaresan, *Metastatic disease of the spine.* Clin Orthop Relat Res, 1982(169): p. 95-102.

9. Maccauro, G., et al., *Physiopathology of spine metastasis.* Int J Surg Oncol, 2011. **2011**: p. 107969.

10. Li, S., et al., *Estimated number of prevalent cases of metastatic bone disease in the US adult population.* Clin Epidemiol, 2012. **4**: p. 87-93.

11. Cecchini, M.G., et al., *Molecular and Biological Mechanisms of Bone Metastasis.* EAU Update Series, 2005. **3**(4): p. 214-226.

12. Coleman, R.E., *Clinical features of metastatic bone disease and risk of skeletal morbidity.* Clin Cancer Res, 2006. **12**(20 Pt 2): p. 6243s-6249s.

13. Gdowski, A.S., A. Ranjan, and J.K. Vishwanatha, *Current concepts in bone metastasis, contemporary therapeutic strategies and ongoing clinical trials.* J Exp Clin Cancer Res, 2017. **36**(1): p. 108.

14. Roudier, M.P., et al., *Histopathological assessment of prostate cancer bone osteoblastic metastases.* J Urol, 2008. **180**(3): p. 1154-60.

15. American Cancer Society. *Cancer Facts & Figures 2017*. 2017.

16. Selvaggi, G. and G.V. Scagliotti, *Management of bone metastases in cancer: a review.* Crit Rev Oncol Hematol, 2005. **56**(3): p. 365-78.

17. Jegoux, F., et al., *Radiation effects on bone healing and reconstruction: interpretation of the literature.* Oral Surg Oral Med Oral Pathol Oral Radiol Endod, 2010. **109**(2): p. 173-84.

18. Steenland, E., et al., *The effect of a single fraction compared to multiple fractions on painful bone metastases: a global analysis of the Dutch Bone Metastasis Study.* Radiotherapy and Oncology, 1999. **52**(2): p. 101-109.

19. Haidukewych, G.J., *Metastatic disease around the hip: maintaining quality of life.* J Bone Joint Surg Br, 2012. **94**(11 Suppl A): p. 22-5.

20. Mirels, H., *Metastatic disease in long bones. A proposed scoring system for diagnosing impending pathologic fractures.* Clin Orthop Relat Res, 1989(249): p. 256-64.

21. Nielsen, O.S., A.J. Munro, and I.F. Tannock, *Bone metastases: pathophysiology and management policy.* J Clin Oncol, 1991. **9**(3): p. 509-24.

22. Damron, T.A., et al., *Critical evaluation of Mirels' rating system for impending pathologic fractures.* Clin Orthop Relat Res, 2003(415 Suppl): p. S201-7.

23. Damron, T.A., et al., *CT-based Structural Rigidity Analysis Is More Accurate Than Mirels Scoring for Fracture Prediction in Metastatic Femoral Lesions.* Clin Orthop Relat Res, 2016. **474**(3): p. 643-51.

24. Miller, B.J., *Neoplasia-Metastatic Disease of the Skeleton*. 2015.

25. Bhatti, M.A., *Advanced topics in finite element analysis of structures : with Mathematica and MATLAB computations*. 2006, Hoboken, N.J.: John Wiley. xvi, 590 p.

26. Gupta, K.K. and J.L. Meek, *A BRIEF HISTORY OF THE BEGINNING OF THE FINITE ELEMENT METHOD.* International Journal for Numerical Methods in Engineering, 1996. **39**(22): p. 3761-3774.

27. Huiskes, R. and E.Y. Chao, *A survey of finite element analysis in orthopedic biomechanics: the first decade.* J Biomech, 1983. **16**(6): p. 385-409.

28. Bonneau, N., O. Gagey, and C. Tardieu, *Biomechanics of the human hip joint.* Comput Methods Biomech Biomed Engin, 2012. **15 Suppl 1**: p. 197-9.

29. Anderson, L.C. and D.J. Blake, *The anatomy and biomechanics of the hip joint.* J Back Musculoskelet Rehabil, 1994. **4**(3): p. 145-53.

30. Schilders, E. *Hip Anatomy*. 2014; Available from: http://ernestschilders.com/hip-anatomy.php.

31. Medicus, L. *Femur Knee Lower Leg Anatomy*. 2017; Available from: http://anatomy.lexmedicus.com.au/pathologies/knee.

32. Trammell, L.H. and A.M. Kroman, *Chapter 13 - Bone and Dental Histology A2 - DiGangi, Elizabeth A*, in *Research Methods in Human Skeletal Biology*, M.K. Moore, Editor. 2013, Academic Press. p. 361-395.

33. Zenger, I. *The History of Computed Tomography at Siemens*. 2015.

34. Lotz, J.C., E.J. Cheal, and W.C. Hayes, *Fracture prediction for the proximal femur using finite element models: Part I--Linear analysis.* J Biomech Eng, 1991. **113**(4): p. 353-60.

35. Keyak, J.H., et al., *Prediction of femoral fracture load using automated finite element modeling.* Journal of Biomechanics, 1997. **31**(2): p. 125-133.

36. Keyak, J.H., et al., *Prediction of fracture location in the proximal femur using finite element models.* Med Eng Phys, 2001. **23**(9): p. 657-64.

37. Keyak, J.H. and S.A. Rossi, *Prediction of femoral fracture load using finite element models: an examination of stress- and strain-based failure theories.* J Biomech, 2000. **33**(2): p. 209-14.

38. Keyak, J.H., et al., *Automated three-dimensional finite element modelling of bone: a new method.* J Biomed Eng, 1990. **12**(5): p. 389-97.

39. Keyak, J.H., et al., *The effect of simulated metastatic lytic lesions on proximal femoral strength.* Clin Orthop Relat Res, 2007. **459**: p. 139-45.

40. Derikx, L.C., et al., *The assessment of the risk of fracture in femora with metastatic lesions: comparing case-specific finite element analyses with predictions by clinical experts.* J Bone Joint Surg Br, 2012. **94**(8): p. 1135-42.

41. Goodheart, J.R., et al., *Simulating activities of daily living with finite element analysis improves fracture prediction for patients with metastatic femoral lesions.* J Orthop Res, 2015. **33**(8): p. 1226-34.

42. Bergmann, G., et al., *Hip contact forces and gait patterns from routine activities.* J Biomech, 2001. **34**(7): p. 859-71.

43. Damm, P. and A. Bender. *Data Collection 'HIP98'*. 1998 2017; Available from: https://orthoload.com/test-loads/data-collection-hip98/.

44. Permeswaran, P.T., B.J. Miller, and J.E. Goetz, *Mechanics-Based Fracture Risk Correlates Poorly with Mirels' Score in Metastatic Lesions to the Proximal Femur*, in *Orthopaedic Research Society*. 2017: San Diego, CA.

45. Permeswaran, P.T., B.J. Miller, and J.E. Goetz, *Mechanics-Based FractureRisk Under Gait Cycle Loading Correlates Poorly with High Mirels' Scores in Metastatic Lesions to the Proximal Femur*, in *Midwest American Society of Biomechanics*. 2017: Grand Rapids, MI.

46. Permeswaran, P.T., B.J. Miller, and J.E. Goetz, *Localized Fracture Risk Under Gait Cycle Loading Correlates Poorly with High Mirels' Scores in Metastatic Lesions to the Proximal Femur*, in *American Society of Biomechanics*. 2017: Boulder, CO.

47. Ahmadi, S., et al., *The biomechanics of three different fracture fixation implants for distal femur repair in the presence of a tumor-like defect.* Proc Inst Mech Eng H, 2013. **227**(1): p. 78-86.

48. Sivasundaram, R., et al., *The biomechanical effect of proximal tumor defect location on femur pathological fractures.* J Orthop Trauma, 2013. **27**(8): p. e174-80.

49. Walmsley, D., et al., *Biomechanical analysis of the cephalomedullary nail versus the trochanteric stabilizing plate for unstable intertrochanteric femur fractures.* Proc Inst Mech Eng H, 2016.

50. Lai, P.L., et al., *Chemical and physical properties of bone cement for vertebroplasty*. Biomed J, 2013. **36**(4): p. 162-7.

51. Zdero, R., et al., *A biomechanical comparison of four different cementless press-fit stems used in revision surgery for total knee replacements.* Proc Inst Mech Eng H, 2012. **226**(11): p. 848-57.

52. Davy, D.T., et al. *Nonlinear Stress-Strain Behavior due to Damage Accumulation in Cortical Bone*. in *IUTAM Symposium on Synthesis in Bio Solid Mechanics*. 1998. Copenhegen, Denmark.

53. Medicine, N.L.o. *Visible Human Project*. 2015 May 28, 2015; Available from: https://www.nlm.nih.gov/research/visible/getting_data.html.

54. Goetz, J.E., *Critical Aspects of Modeling Femoral Head Osteonecrosis in the Emu*, in *Department of Biomedical Engineering*. 2008, University of Iowa: Iowa City, IA.

55. Vivanco, J.F., et al., *Estimating the density of femoral head trabecular bone from hip fracture patients using computed tomography scan data.* Proc Inst Mech Eng H, 2014. **228**(6): p. 616-626.

56. Keyak, J.H., I.Y. Lee, and H.B. Skinner, *Correlations between orthogonal mechanical properties and density of trabecular bone: use of different densitometric measures.* J Biomed Mater Res, 1994. **28**(11): p. 1329-36.

57. Reilly, D.T. and A.H. Burstein, *The elastic and ultimate properties of compact bone tissue.* J Biomech, 1975. **8**(6): p. 393-405.

58. Parekh, J., et al., *In vitro investigation of friction at the interface between bone and a surgical instrument.* Proc Inst Mech Eng H, 2013. **227**(6): p. 712-8.

59. Baker, K.J., T.D. Brown, and R.A. Brand, *A finite-element analysis of the effects of intertrochanteric osteotomy on stresses in femoral head osteonecrosis.* Clin Orthop Relat Res, 1989(249): p. 183-98.

60. Bayraktar, H.H., et al., *Comparison of the elastic and yield properties of human femoral trabecular and cortical bone tissue.* Journal of Biomechanics, 2004. **37**(1): p. 27-35.

61. von Mises, R.E., *Mechanics of Solid Bodies in the Plastically-Deformable State*. 1913. p. 582-592.

62. Schileo, E., et al., *Subject-specific finite element models implementing a maximum principal strain criterion are able to estimate failure risk and fracture location on human femurs tested in vitro.* J Biomech, 2008. **41**(2): p. 356-67.

63. Morris, J., *Amyotrophic Lateral Sclerosis (ALS) and Related Motor Neuron Diseases: An Overview.* Neurodiagn J, 2015. **55**(3): p. 180-94.

64. Courtney, A.C., et al., *Effects of loading rate on strength of the proximal femur.* Calcif Tissue Int, 1994. **55**(1): p. 53-8.

65. Bhardwaj, A., A. Gupta, and T. Kwong Ming. *Mechanical response of femur bone to bending load using finite element method*. in *2014 Recent Advances in Engineering and Computational Sciences (RAECS)*. 2014.